Ultrasensitive Detection of Xylene Gas by Cauliflower-like Au-TiO_2 Core-Shell Nanoparticles

Hyeong Min Kim[a,1], Ka Yoon Shin[a,1], Ali Mirzaei[b,*], Wansik Oum[a], Eun Bi Kim[a], Sungjoon Moon[a], Somalapura Prakasha Bharath[c], Sang Sub Kim[d,*], Hyoun Woo Kim[a,e,*]

[a]*Division of Materials Science and Engineering, Hanyang University, Seoul, 133-791, Republic of Korea*

[b]*Department of Materials Science and Engineering, Shiraz University of Technology, Shiraz, Iran*

[c]*Catalan Institute of Nanoscience and Nanotechnology (ICN2), CSIC and BIST, Campus UAB, Bellaterra, 08193 Barcelona, Spain*

[d]*Department of Materials Science and Engineering, Inha University, Incheon, 402-751, Republic of Korea*

[e]*The Research Institute of Industrial Science, Hanyang University, Seoul, 133-791, Republic of Korea*

[*]Corresponding Authors: mirzaei@sutech.ac.ir (A.M), sangsub@inha.ac.kr (S.S.K), hyounwoo@hanyang.ac.kr (H.W.K)

[1] Equal contributions

Abstract

TiO_2 nanoparticles (NPs) and Au-TiO_2 core-shell NPs (C-S NPs) were synthesized for xylene gas detection. Morphological, phase, and chemical studies demonstrated the successful generation of Au-TiO_2 C-S NPs with a cauliflower-like morphology and desired composition. Also, the surface area of TiO_2 NPs was 8.46, which increased to 23.88 m^2/g for Au-TiO_2 C-S NPs, due to the creation of a porous TiO_2 shell around the Au core. The response of the TiO_2 NPs to 50 ppm xylene was 14.19 at 500°C, while it increased to 165.77 at a lower temperature (450°C). Furthermore, while the TiO_2 NPs gas sensor has no selectivity to xylene gas, the TiO_2 C-S NP gas sensor exhibited excellent selectivity. Overall, incorporation of Au in TiO_2 in the form of a C-S structure improved the performance of the sensor to sense xylene. Improved xylene sensing for the TiO_2 C-S NPs stemmed from the high surface area and porous nature, oxygen defects, and formation of Au-TiO_2 Schottky barriers. This research demonstrates the development of high-output xylene sensors by means of Au-TiO_2 with a C-S structure.

Keywords: Xylene; Au-TiO_2; Core-shell; Gas sensor; Selectivity; Sensing mechanism.

1. Introduction

Volatile organic compounds (VOCs) are highly volatile in nature at room temperature (20°C) and 1 atm [1]. Benzene (C_6H_6), toluene (C_7H_8), and xylene (C_8H_{10}), collectively known as BTX, are among the most common VOCs and are generally found in petroleum products [2,3]. Among the three isomers of xylene (meta(*m*), ortho (*o*), and para (*p*)) [4], *p*-xylene, which is a flammable and colorless liquid, comprises ~86 vol% of the overall consumption of xylene. *p*-xylene is utilized in a cleaning agent, solvent, and starting material for synthesis of terephthalic acid used in the synthesis of polyester fibers and resins [5,6].

However, xylene is considered a pollutant and toxic VOC [7]. Inhaling xylene vapors causes irritation of the throat and nose as well as difficulty in breathing. Neural toxicity includes slight inebriation, headaches, dizziness, irritability, vertigo, staggering, and unconsciousness. Furthermore, it can negatively affect the kidneys, liver, and central nervous system. Renal toxicity effects include nausea, abdominal pain, and vomiting [8]. Furthermore, xylene is a biomarker for fast detection of prostate cancer [9]. Therefore, detection of xylene is of importance in multiple aspects.

Even though traditional approaches like gas chromatography and ion/mass spectrometry techniques may be used for detection of VOCs, in general, they need complicated and tedious pre-treatment procedures. Furthermore, they are not portable and consume high power [10]. Therefore, gas sensors with online response, portability, and high performance can be used for detection of VOCs including xylene. Among sensors, the resistive type is popular due to its quick response time (t_{res}) and recovery time (t_{rec}), high response, good stability, simplicity in manufacturing, and affordable price [11]. Generally, semiconducting metal oxides are employed for realization of

resistive sensors owing to simple synthesis, stable nature, low cost , and high mobility of charge carriers [12].

N-type TiO_2 is a wide band gap semiconductor that crystalizes in three phases: rutile, brookite, and anatase. Among them, rutile is the most stable [13]. With its transparency to visible light, strong oxidizing ability for decomposition of organic substances, good superhydrophilicity, high stability, nontoxicity, and low cost [14], TiO_2 is not only widely used in photocatalyst applications [15,16], but is also a promising sensing material [17]. However, in their pristine form, TiO_2 gas sensors have high sensing temperatures, low response, and poor selectivity [18]. Hence, various approaches such as p-n heterojunction [19,20], doping [21,22], decoration [23,24], and use of special morphologies like core-shell (C-S) structures [25,26] have suggested to boost the sensing characteristics of TiO_2 sensors including a decrease of sensing temperature, boosting of response, and selectivity enhancement.

In C-S structures, a thin layer of shell material is present around a core, and the interface area between the two materials is maximized [27]. For gas sensing applications, the two most widely used C-S structures are metal oxide-metal oxide [28,29] as well as noble metal-metal oxide [30] [31]. In particular, the use of the latter C-S structure is highly promising since it prevents direct contact of noble metals with one another due to the presence of an overlying thin shell. In fact, when noble metals are dispersed on metal oxides, they can be easily poisoned by sulfur-containing gases; in cases of poor dispersion or high concentration, these metals can provide conducting paths on the sensor surface and degrade the electrical properties [32].

Previously, Zhu *et al*. [33] reported Au-TiO_2 C-S for successful detection of ozone at room temperature (RT). Kim *et al*. [34] used Au-TiO_2 C-S for CO sensing at 600°C. Also, Park *et al*. [35] used Au-TiO_2 C-S for CO detection. Ag-TiO_2 C-S nanowires were used for detection of NH_3

gas [36]. Zhu *et al*. [37] used Au-TiO_2 C-S for RT sensing of ethanol gas. Liu *et al*. reported a lotus-like Au-TiO_2 sensor for enhanced CO gas sensing [38].

In general, noble metals in combination with metal oxides are used for detection of gases, mainly thanks to their high catalytic activity [39]. Even though Au has higher price relative to other noble metals, its catalytic activity towards p-xylene is already demonstrated in some previous literature [40-42]. However, no studies have been devoted to xylene sensing using an Au-TiO_2 C-S structure.

Motivated by the above, this study produced TiO_2 nanoparticles (NPs) and Au-TiO_2 C-S NPs hydrothermally. The highest response of the TiO_2 NPs sensor to 50 ppm xylene was 14.19 at 500°C, while that for the Au-TiO_2 C-S NPs sensor was higher at 165.77 at a lower temperature (450°C). Besides, the Au-TiO_2 C-S NP gas sensor exhibited excellent selectivity to xylene, while the TiO_2 NP gas sensor did not. The boosted xylene detection capability of the Au-TiO_2 C-S NP sensor was ascribed to its high surface area and porous nature, oxygen defects, and formation of Au-TiO_2 Schottky barriers.

2. Experimental Section

2.1. Chemicals

Gold (III) chloride trihydrate (HAuCl4, 99.9% purity), titanium (Ⅳ) fluoride (TiF_4), and L-ascorbic acid ($C_6H_8O_6$, 98% purity) were purchased from Sigma-Aldrich. Trisodium citrate dehydrate ($Na_3C_6H_5O_7{\cdot}2H_2O$, 99.0% purity) was purchased from Alfa Aesar Co.

2.2. Synthesis of Au-TiO_2 C-S NPs

Fig. 1 schematically depicts the production of Au-TiO_2 C-S NPs. Initially, a $HAuCl_4$ solution (250 mL, 1 mM) was heated while stirring. Later on, the above solution was subjected to stirring again at 100℃ for 5 min after the addition of a trisodium citrate solution (4.5 mL, 10 mM). Subsequently, the gradual introduction of substance ascorbic acid (0.01 M, 4 mL) into the solution above resulted in a transformation of color to purple. Then, TiF_4 (0.04 M, 6 mL) was added to the solution, and DI water was added to dilute the mixture to 80 mL. An autoclave was filled with this solution and processed at 180ºC for 48 h. Then, the cooled solution was washed with DI water using centrifugation at 8,000 rpm for 15 min and was dried in an oven. For production of pristine TiO_2 NPs, the same procedure was employed without $HAuCl_4$.

2.3. Characterizations

Scanning electron microscopy (SEM; Hitachi S-4200,) and transmission electron microscopy (TEM; JEM-2100 F, JEOL) were used for morphological examination. The chemical composition exploration was carried out using Energy-dispersive X-ray spectroscopy (EDS) in TEM. To ascertain the powder phases, X-ray diffraction (XRD) was performed with $CuK_{\alpha 1}$ radiation (λ = 0.15406 nm) using a Bruker D8 Advance instrument. The Brunauer-Emmett-Teller (BET) surface area was obtained by N_2 adsorption-desorption analysis (Star II 3020, Micromeritics Instrument Corporation). To obtain information on the elemental chemical states, X-ray photoelectron spectroscopy (XPS; Thermo Fisher Scientific) was conducted. Ultraviolet photoelectron spectroscopy (UPS, Thermo Fisher Scientific) analysis in ultrahigh vacuum using HeI (hν=21.2 eV) radiation was employed to calculate the work functions.

2.4. Gas sensing tests

A bi-layer (Au-Ti) electrode was sputter-deposited onto an Al_2O_3 substrate as a gas sensor (**Fig. 1**). To evaluate the electrical and gas sensing behavior of the sensors, they were positioned within a gas chamber in a tubular quartz furnace having good temperature control. The gases (xylene, NO_2, CO, C_2H_4, N_2O, CO_2, H_2S, H_2, CH_3COCH_3, toluene, and benzene) in their standard cylinders had an initial concentration of 100 ppm, while the background consisted of dry air with no relative humidity (0% RH). Also, NH_3 used N_2 as a background gas. Synthetic dry air was used as a balance gas to make desired concentrations of gases. For all the gases, except NH_3, a mixture of pure air and target gas from cylinders balanced with dry air were inserted into the chamber via mass flow controllers (MFCs), while keeping a constant flow rate of 100 sccm into gas chamber. The xylene sensing behaviors were also examined in humid air (RH up to 80%) at 450^{o}C. The genuine temperature and specific RH values were gauged employing the commercial RH probe. To attain 100% relative humidity (RH) in the air, dry air was introduced into a sealed glass vessel containing water. Thereby, bubbles in the air were formed and directed toward the outlet line. By blending dry air (0% RH) with humid air (100% RH) at suitable levels using MFCs, the RH level was controlled (e. g., 3:2 ratio for 40% RH and 1:4 ratio for 80% RH). The resistance of the gas sensors was dynamically measured in the air (R_a) and target gas (R_g). The response was computed as $R=R_a/R_g$ for reducing gases and as $R=R_g/R_a$ for oxidizing gases. The t_{res} and t_{rec} were obtained using the procedure in [43].

3. Results and discussion

3.1. Structural, morphological, and compositional studies

Figs. 2(a)-(c) give TEM micrographs of the Au-TiO_2 C-S NPs. A C-S structure was obtained with a core size of ~ 50 nm and overall C-S NP size 300 nm. The shell was not smooth but contained voids and pores, which are advantageous for gas diffusion. Also, **Figs. S1(a)-(d)** display additional TEM images of multiple Au-TiO_2 C-S, revealing the spherical morphology of the Au core in the synthesized Au-TiO C-S with an average Au size of approximately 50 nm. **Fig. 2(d)** indicates the selected area electron diffraction (SAED) pattern of the Au-TiO_2 C-S NPs. Rings related to the (111), (200), and (222) crystalline planes of Au [44] and to the (116), (105), and (101) crystalline planes of TiO_2 [45] were seen, confirming the co-existence of Au and TiO_2. To determine the chemical composition of NPs, TEM-EDS color mapping analysis was performed. **Figs. 2(e)-(h)** show the combined mapping, mapping of Ti, mapping of O, and mapping of Au elements, respectively. The core part was comprised of Au, while the shell part was TiO_2. Also, the EDS spectrum in **Fig. 2(i)** presents the expected signals related to Ti, O, and Au, at weight percentages of 62.28, 29.57, and 8.15%, respectively. **Fig. 3(a)** shows XRD pattern of Au-TiO_2 C-S NPs, exhibiting the peaks related to Au core, which match with JCPDS File No. 04-0784 (**Fig. 3(d)**), along with the peaks related to TiO_2 (anatase) (JCPDS File 21-1272 (**Fig. 3(c)**). Also, in **Fig. 3(b)**, XRD pattern of bare TiO_2 is presented, well matching with the anatase phase of TiO_2. **Figs. 3(e) and (f)** display SEM images of TiO_2 NPs at two magnifications, demonstrating a rectangular-like morphology with sizes of 100-500 nm. **Figs. 3(g) and (h)** present SEM micrographs of Au-TiO_2 C-S NPs at two magnifications. Similar to a recent study [46], the NPs had a cauliflower-like morphology comprised of individual Au cores with sizes of 50 nm and an overall C-S size of ~300 nm.

Figs. 4(a) and (b) reveal the BET graphs of TiO_2 NPs and Au-TiO_2 C-S NPs, respectively, with BET surface areas of 8.46 and 23.88 m^2/g. This confirms that the surface area of Au-TiO_2 C-S NPs

was almost three times that of the TiO_2 NPs, demonstrating the porous nature of the TiO_2 shell around individual Au NPs, as observed in the TEM analysis. Therefore, increase of surface area after formation of C-S structure can be related to formation of porous TiO_2 shell. Also, **Figs. 4(c) and (d)** reveal the BJH curves of TiO_2 NPs and Au-TiO_2 C-S NPs, respectively. Based on the BJH plots, the average sizes of pores in TiO_2 NPs and Au-TiO_2 C-S NPs were 41.68 and 559.22 nm, respectively. The larger pores in Au-TiO_2 C-S NPs provide a higher surface area for channels of gas diffusion [47].

Fig. 5(a) shows the XPS survey of Au-TiO_2 C-S NPs, comprising signals related to C (from the environment), Ti, O, and Au. Lack of impurity signals in the XPS survey, demonstrating high purity of starting precursors and successful synthesis. **Fig. 5(b)** reveals the Au 4f core-level region peaks of Au $4f_{7/2}$ and Au $4f_{5/2}$ at 83.2 and 86.9 eV, respectively, which can be ascribed to metallic Au [48]. Also, **Fig. 5(c)** reveals the Ti 2p core region, with two peaks at 459.4 and 465.3 eV, related to Ti $2p_{3/2}$ and Ti $2p_{1/2}$, respectively [49]. **Fig. 5(d)** displays deconvoluted O 1s, where three peaks corresponding to lattice oxygen (O_l) at 530.0 eV, oxygen vacancies (O_v) at 531.2 eV, and adsorbed oxygen at 532.1 eV [50] are accurately fitted. The areas of these peaks were 66.5, 7.2, and 26.3%, respectively, showing that considerable oxygen was adsorbed on the Au-TiO_2 C-S NPs, which is an advantage for reaction with xylene gas [51].

To calculate the work function (Φ) of the synthesized materials, UPS spectra were obtained for Au and TiO_2 NPs, as presented in **Fig. 6(a)**. Based on the energy cut-off values of Au and TiO_2 NPs presented in **Figs. 6(b) and (c)**, respectively, Φ values were calculated using the procedure explained in a recent paper and were 5.2 and 5.0 eV for Au and TiO_2 NPs [52].

3.2. Gas sensing part

Fig. 7(a) offers the responses of TiO_2 and Au-TiO_2 C-S NPs sensors to xylene (50 ppm) according to temperature. At lower temperatures, the resistance of the gas sensors was very high due to wide band gap of TiO_2 and low mobility of charge carriers. Also, at lower temperatures, the responses of both gas sensors were very low due to the insufficient energy of xylene to overcome the adsorption potential barrier. At 300°C, the responses of TiO_2 and Au-TiO_2 C-S NPs sensors were 1.00 and 2.88, respectively. For TiO_2 NPs, the response gradually increased with temperature, reaching the highest response of 14.19 at 500°C. For the Au-TiO_2 C-S NP gas sensor, the maximum response was observed at 450°C, and a further increase of temperature to 500°C decreased the response as the desorption rate became dominant over the adsorption rate. Also, **Figs. 7(b) and (c)** present the changes in the base resistance of TiO_2 and Au-TiO_2 C-S sensors with temperature, respectively. In both instances, the resistance decreases as the temperature rises, indicating a semiconducting nature. An increased number of electrons transition from the valence band of TiO_2 to the conduction band, causing a reduction in the base resistance. Also, under the identical temperatures, the base resistance of Au@TiO_2 C-S nanocomposite surpasses that of pure TiO_2. This is because electrons shift from TiO_2 to Au owing to the variance in the work function of two materials.

Figs. 8(a) and (b) reveal the transient resistance plots of TiO_2 and Au-TiO_2 C-S NPs, respectively, to 10, 30, and 50 ppm xylene at their optimal sensing temperatures. In both cases, the resistance dropped in the presence of reducing xylene gas, revealing the n-type nature originating from TiO_2. The base resistance of TiO_2 NPs was lower than that of Au-TiO_2 C-S NPs, reflecting the flow of electrons from TiO_2 to Au. To obtain better insight, the transient response graphs of the two sensors to various amounts of xylene gas are compared in **Fig. 8(c)**. The responses of the

TiO_2 NP gas sensor to 10, 30, and 50 ppm xylene were 3.78, 5.82, and 7.27, respectively, and those of the Au-TiO_2 C-S NP gas sensor were 63.38, 97.91, and 165.77 (**Fig. 8(d)**). This shows that incorporation of Au into TiO_2 in the form of a C-S structure remarkably increased the response of the sensor to xylene gas, implying a promising role of Au NPs toward xylene gas sensing due to their catalytic effects and electronic features. Besides, the t_{res} and t_{rec} of the Au-TiO_2 C-S NP sensor to 50 ppm xylene were 458 and 345 s, respectively (**Figs. S2(a) and (b)**).

To assess the output of the Au-TiO_2 C-S NP sensor to low amounts of xylene gas, it was exposed to 1, 3, 5, 7, and 9 ppm xylene at 450°C (**Fig. 9(a)**). The relevant calibration graph is shown in **Fig. 9(b)**. The responses to the mentioned concentrations were 2.0, 5.6, 15.4, 31.3, and 57.2, respectively, demonstrating successful xylene detection. The sensors were exposed to NO_2, CO, C_2H_4, NH_3, N_2O, CO_2, H_2S, H_2, CH_3COCH_3, toluene, benzene, and xylene gases (50 ppm) at 450°C for selectivity studies (**Fig. 9(c)**). The responses of TiO_2 NPs to the mentioned gases were 1.47, 2.77, 2.30, 2.52, 2.74, 2.47, 5.39, 2.51, 2.57, 1.43, 1.48, and 7.27, respectively. The responses of the Au-TiO_2 C-S NP sensor to the mentioned gases were 1.00, 1.53, 1.79, 1.88, 1.93, 2.21, 5.11, 5.59, 19.17, 1.41, 2.24, and 165.77, respectively. These results show that the TiO_2 NP sensor had no selectivity for xylene, while the Au-TiO_2 C-S NP gas sensor showed high selectivity to xylene gas, which is important from a practical viewpoint. **Fig. 9(d)** shows the response of the Au-TiO_2 C-S NP toward 50 ppm xylene at 450°C in the humid air. The responses in 40 and 80% RH were decreased to 81.2 and 52.0% of the response in dry air, respectively. In humid air, H_2O molecules adhere to the sensor and occupied potential adsorption sites, decreasing the number of sites for xylene adsorption [53]. In order to avoid the decrease of the response in humid environments, we may add moisture-proof barriers for hygroscopic materials [54]. For example, some MOFs with good hydrophobicity can increase moisture-proof nature of gas sensors [55].

Fig. 9(e) illustrates the repeatability of Au-TiO_2 C-S NPs gas sensor over five consecutive cycles when subjected to 50 ppm xylene at 450°C. The responses calculated across sensing cycles are presented in **Fig. 9(f)**. **Fig. 9(g)** displays the reproducibility evaluation of these three fabricated Au-TiO_2 C-S NP gas sensors when exposed to 50 ppm xylene at 450°C. **Fig. 9(h)** illustrates the sensing cycles for both the newly fabricated and stored (after six months) sensors to 50 ppm xylene gas at 450°C. The response showed a slight decline from 165.77 in its initial state to 161.19 after six-month period, indicating excellent stability.

There are three types of xylene isomers depending on the position of $–CH_3$ group on the benzene ring of xylene as shown in **Fig. S3(a)**. Among them, p-xylene occupies about 86% of consumption in volume [5]. Therefore, we also exposed the sensor to o-and m-xylene gases at 450°C (**Fig. S3(b)**). The response to 50 ppm o- and m-xylene gases was 4.04 and 5.74 respectively, which were insignificant comparted to the response to p-xylene (165.77).

In real applications, microheaters are installed on the sensor devices, elevating the sensing temperature to desired temperatures (>300°C). Since the heating part is relatively small in comparison to sensing systems, it will not significantly warm the surroundings: In canned sensors, the sensing part with the micro-heater pattern is located inside the metallic can, which is situated > 5 mm above the circuit board. In MEMS or NEMS sensors, the sensing part itself is extremely small [56]. By the way, the relatively high sensing temperature may result is relatively high power consumption. Sensing temperature can be reduced by operation of the sensor in self-heating mode [11] or use of UV light irradiation [57], which will be studied in future works.

3.3 Proposed sensing mechanism

The mechanism of adsorption of oxygen molecules onto TiO_2 NPs in air is shown below [58].

$$O_{2(gas)} \rightarrow O_{2(ads)} \quad (1)$$

$$O_{2(ads)} + e^- \rightarrow O_{2(ads)}^- \quad (2)$$

$$O_{2(ads)}^- + e^- \rightarrow 2O^- \quad (3)$$

$$O^- + e^- \rightarrow O^{2-} \quad (4)$$

Since the sensing temperature for TiO_2 NPs was 450°C, we can surmised that the dominant ions on the sensing layer is O^{2-} ions [59]. An insufficiency of electrons on the external surfaces of the TiO_2 NPs led to the generation of an electron depletion layer on TiO_2 NPs. Accordingly, the resistance increased for TiO_2 as an n-type gas sensor [60]. In xylene gas atmosphere, the reaction between adsorbed xylene and oxygen occurs as follows [61].

$$(C_8H_{10})_{ads} + 2O^{2-}(ads) \rightarrow (C_8H_8O) + H_2O + 4e^- \quad (5)$$

$$(C_8H_8O) + 2O^{2-}(ads) \rightarrow CO_2 + H_2O(g) + 4e^- \quad (6)$$

Thus, the released electrons increase the conductivity of the sensor. Moreover, at contact points between individual TiO_2 NPs, homojunctions were formed in air; subsequent exposure to xylene gas decreased the height of the homojunctions, leading to a sensing signal [62]. Anyway, the pristine sensor offered a weak response to xylene due to its small surface area and lack of heterojunctions.

In contrast, the Au-TiO_2 C-S NP gas sensor showed a significantly stronger response to xylene gas. This sensor had a higher surface area (almost three times higher) than that of TiO_2 NPs, with a higher porous nature of the TiO_2 shell layer over the Au NPs. Therefore, the presence of more adsorption sites along these pores led to higher adsorption and better gas diffusion into the deep regions of the sensor (**Fig. 10**).

Owing to the difference in Φ values of Au (Φ=5.2 eV) and TiO_2 (Φ=5 eV), which were calculated based on UPS spectra, Schottky junctions were formed at contact areas between these materials. The energy levels of Au and TiO_2 before contact are presented in **Fig. 11(a)**. Upon contact to rebalance the two Fermi levels, electrons flow from TiO_2 to Au, forming Schottky junctions in air (**Fig. 11(b)**). Therefore, the base resistance of Au-TiO_2 is higher than that of TiO_2 NPs due to the formation of EDL in contact areas with Au. In a xylene environment, the electrons are return to the sensor surface, decreasing the heights of Schottky junctions and the resistance modulation (**Fig. 11(c)**). A higher initial resistance, i.e., smaller electron conduction volume, will contribute to the high sensing behaviors, in which a change of the same electron concentration by introduction of xylene lead to a higher response. Due to numerous Au-TiO_2 C-S NPs, this mechanism is dominant in resistance modulation for this gas sensor.

Noble metals generally have good catalytic activity [63,64]. Also, Au has shown good catalytic performance [65,66]. The dehydrogenation of oxidized $–CH_3$ groups of xylene is catalyzed by adsorbed oxygen species. The catalytic activation of Au in Au NPs can decrease the enthalpy of dehydrogenation of xylene, decreasing the activity while increasing the sensing reaction to produce an improved output. Both plane structure and the π-conjugate of the benzene ring lead easy reaction of xylene with oxygen species absorbed in the Au-TiO_2 gas sensor rather than other gases, which explains the selectivity of the sensor to xylene [67]. Furthermore, incoming oxygen molecules can be adsorbed onto Au NPs to become dissociated on its surface and by a spillover effect [68], move to nearby TiO_2, causing faster and higher adsorption of oxygen ions onto TiO_2 NPs.

Table 1 [61,67,69-77] shows a comparison of the xylene detection capability of the current sensor with those previous research. Overall, the Au-TiO_2 C-S NPs sensor has better performance

than other reported sensors. The relatively high operating temperature may be reduced by strategies such as self-heating operation [78] and UV illumination [79]. It should be noted that recently flexible sensing devices have gained much more attention [80,81], therefore, in future studies, development of flexible sensor based on Au-TiO_2 C-S NPs may open a new opportunity of emerging applications.

4. Conclusions

We demonstrated that incorporation of Au into TiO_2 in the form of a C-S structure improved the performance of a sensor to xylene gas. TiO_2 NPs and Au-TiO_2 C-S NPs were hydrothermally produced for xylene gas detection. TEM/SEM investigations confirmed the formation of Au-TiO_2 C-S NPs with a cauliflower-like morphology and high surface area of 23.88 m^2/g along with a desired composition. Also, the surface area of TiO_2 NPs was 8.46, and it increased for Au-TiO_2 C-S NPs due to the creation of a porous TiO_2 shell around the Au core. The response of the TiO_2 NP sensor to 50 ppm xylene was 14.19 at 500°C, and that for the Au-TiO_2 C-S NP sensor was higher at 165.77 at 450°C. Furthermore, while the TiO_2 NP gas sensor has no selectivity to xylene, the Au-TiO_2 C-S NP gas sensor demonstrated outstanding selectivity. The porous nature and high surface area, oxygen defects, and formation of Au-TiO_2 Schottky barriers accounted for the boosted xylene detection of the Au-TiO_2 C-S NPs.

Acknowledgement

This project was provided by the Basic Science Research Program through the National Research Foundation of Korea (NRF) funded by the Ministry of Education

(2016R1A6A1A03013422). This project was provided by a National Research Foundation of Korea (NRF) grant funded by the Korean government (MSIT) (RS-2023-00247528 and 2021R1A2C1009790).

References

[1] P.C. Moura, M. Raposo, V. Vassilenko, Breath Volatile Organic Compounds (VOCs) as Biomarkers for the Diagnosis of Pathological Conditions: A Review, Biomed. J. 46 (2023) 100623, https://doi.org/10.1016/j.bj.2023.100623.

[2] A. Mirzaei, J.-H. Kim, H.W. Kim, S.S. Kim, Resistive-based gas sensors for detection of benzene, toluene and xylene (BTX) gases: a review, J. Mater. Chem. C 6 (2018) 4342-4370, htts://doi.org/10.1039/C8TC00245B.

[3] M.R. Krishnan, E. Alsharaeh, Potential removal of benzene-toluene-xylene toxic vapors by nanoporous poly (styrene-r-methylmethacrylate) copolymer composites, Environ. Nanotechnol. Monit. Manag. 20 (2023) 100860, https://doi.org/10.1016/j.enmm.2023.100860.

[4] I. Meziane, N. Delort, O. Herbinet, R. Bounaceur, F. Battin-Leclerc, A comparative study of the oxidation of toluene and the three isomers of xylene, Combust. Flame 257 (2023) 113046, https://doi.org/10.1016/j.combustflame.2023.113046.

[5] Q. Shi, J.C. Gonçalves, A.F. Ferreira, A.E. Rodrigues, A review of advances in production and separation of xylene isomers, Chem. Eng. Process. 169 (2021) 108603, https://doi.org/10.1016/j.cep.2021.108603.

[6] W. Duan, F. Meng, F. Wang, Q. Liu, Environmental behavior and eco-toxicity of xylene in aquatic environments: A review, Ecotox. Environ. Safe. 145 (2017) 324-332, https://doi.org/10.1016/j.ecoenv.2017.07.050.

[7] S. Yan, Q. Zhou, Toxic effects of Hydrilla verticillata exposed to toluene, ethylbenzene and xylene and safety assessment for protecting aquatic macrophytes, Chemosphere 85 (2011) 1088-1094, https://doi.org/10.1016/j.chemosphere.2011.07.040.

[8] W.E. Luttrell, Toxic tips: xylene, J. Chem. Health Saf. 19 (2012) 34-35, https://doi.org/10.1016/j.jchas.2012.01.008.

[9] A. Jiménez-Pacheco, M. Salinero-Bachiller, M.C. Iribar, A. López-Luque, J.L. Miján-Ortiz, J.M. Peinado, Furan and p-xylene as candidate biomarkers for prostate cancer, Urologic Oncology: Seminars and Original Investigations, Elsevier (2018) 243. e221-243. e227, https://doi.org/10.1016/j.urolonc.2017.12.026.

[10] A. Mirzaei, S. Leonardi, G. Neri, Detection of hazardous volatile organic compounds (VOCs) by metal oxide nanostructures-based gas sensors: A review, Ceram. Int. 42 (2016) 15119-15141, https://doi.org/10.1016/j.ceramint.2016.06.145.

[11] S.M. Majhi, A. Mirzaei, H.W. Kim, S.S. Kim, T.W. Kim, Recent advances in energy-saving chemiresistive gas sensors: A review, Nano Energy 79 (2021) 105369, https://doi.org/10.1016/j.nanoen.2020.105369.

[12] A. Mirzaei, M.H. Lee, K.K. Pawar, S.P. Bharath, T.-U. Kim, J.-Y. Kim, S.S. Kim, H.W. Kim, Metal oxide nanowires grown by a vapor–liquid–solid growth mechanism for resistive gas-

sensing applications: An overview, Materials 16 (2023) 6233, https://doi.org/10.3390/ma16186233.

[13] Y. Wang, Y. He, Q. Lai, M. Fan, Review of the progress in preparing nano TiO_2: An important environmental engineering material, J. Environ. Sci. 26 (2014) 2139-2177, https://doi.org/10.1016/j.jes.2014.09.023.

[14] K. Nakata, A. Fujishima, TiO_2 photocatalysis: Design and applications, J. Photochem. Photobiol. C-Photochem. Rev. 13 (2012) 169-189, https://doi.org/10.1016/j.jphotochemrev.2012.06.001.

[15] K. Hashimoto, H. Irie, A. Fujishima, TiO_2 photocatalysis: a historical overview and future prospects, Jpn. J. Appl. Phys. 44 (2005) 8269, https://doi.org/10.1143/JJAP.44.8269.

[16] Q. Guo, C. Zhou, Z. Ma, X. Yang, Fundamentals of TiO_2 photocatalysis: concepts, mechanisms, and challenges, Adv. Mater. 31 (2019) 1901997, https://doi.org/10.1002/adma.201901997.

[17] Z. Li, Z. Yao, A.A. Haidry, T. Plecenik, L. Xie, L. Sun, Q. Fatima, Resistive-type hydrogen gas sensor based on TiO_2: A review, Int. J. Hydrog. Energy 43 (2018) 21114-21132, https://doi.org/10.1016/j.ijhydene.2018.09.051.

[18] X. Tian, X. Cui, T. Lai, J. Ren, Z. Yang, M. Xiao, B. Wang, X. Xiao, Y. Wang, Gas sensors based on TiO_2 nanostructured materials for the detection of hazardous gases: A review, Nano Mater. Sci. 3 (2021) 390-403, https://doi.org/10.1016/j.nanoms.2021.05.011.

[19] H. He, C. Zhao, J. Xu, K. Qu, Z. Jiang, Z. Gao, Y.-Y. Song, Exploiting free-standing p-CuO/n-TiO_2 nanochannels as a flexible gas sensor with high sensitivity for H_2S at room temperature, ACS Sens. 6 (2021) 3387-3397, https://doi.org/10.1021/acssensors.1c01256.

[20] O. Alev, E. Şennik, Z.Z. Öztürk, Improved gas sensing performance of p-copper oxide thin film/n-TiO_2 nanotubes heterostructure, J. Alloy. Compd. 749 (2018) 221-228, https://doi.org/10.1016/j.jallcom.2018.03.268.

[21] K. Wu, M. Debliquy, C. Zhang, Room temperature gas sensors based on Ce doped TiO_2 nanocrystals for highly sensitive NH_3 detection, Chem. Eng. J. 444 (2022) 136449, https://doi.org/10.1016/j.cej.2022.136449.

[22] A.K. Vishwakarma, A.K. Sharma, N.K. Yadav, L. Yadava, Development of CdS-doped TiO_2 nanocomposite as acetone gas sensor, Vacuum 191 (2021) 110363, https://doi.org/10.1016/j.vacuum.2021.110363.

[23] X. Li, Y. Zhao, X. Wang, J. Wang, A.M. Gaskov, S. Akbar, Reduced graphene oxide (rGO) decorated TiO_2 microspheres for selective room-temperature gas sensors, Sens. Actuator B-Chem. 230 (2016) 330-336, https://doi.org/10.1016/j.snb.2016.02.069.

[24] H. Liu, W. Shen, X. Chen, A room temperature operated ammonia gas sensor based on Ag-decorated TiO_2 quantum dot clusters, RSC Adv. 9 (2019) 24519-24526, https://doi.org/10.1039/C9RA05439A.

[25] D. Liu, L. Lin, Q. Chen, H. Zhou, J. Wu, Low power consumption gas sensor created from silicon nanowires/TiO_2 core–shell heterojunctions, ACS Sens. 2 (2017) 1491-1497, https://doi.org/10.1021/acssensors.7b00459.

[26] F. Li, X. Gao, R. Wang, T. Zhang, G. Lu, Study on TiO_2-SnO_2 core-shell heterostructure nanofibers with different work function and its application in gas sensor, Sens. Actuator B-Chem. 248 (2017) 812-819, https://doi.org/10.1016/j.snb.2016.12.009.

[27] P.K. Kalambate, Z. Huang, Y. Li, Y. Shen, M. Xie, Y. Huang, A.K. Srivastava, Core@ shell nanomaterials based sensing devices: A review, Trac-Trends Anal. Chem. 115 (2019) 147-161, https://doi.org/10.1016/j.trac.2019.04.002.

[28] Y. Xu, L. Zheng, C. Yang, W. Zheng, X. Liu, J. Zhang, Chemiresistive sensors based on core-shell ZnO@ TiO_2 nanorods designed by atomic layer deposition for n-butanol detection, Sens. Actuator B-Chem. 310 (2020) 127846, https://doi.org/10.1016/j.snb.2020.127846.

[29] S.I. Boyadjiev, O. Kéri, P. Bárdos, T. Firkala, F. Gáber, Z.K. Nagy, Z. Baji, M. Takács, I.M. Szilágyi, TiO_2/ZnO and ZnO/TiO_2 core/shell nanofibers prepared by electrospinning and atomic layer deposition for photocatalysis and gas sensing, Appl. Surf. Sci. 424 (2017) 190-197, https://doi.org/10.1016/j.apsusc.2017.03.030.

[30] P. Rai, S.M. Majhi, Y.-T. Yu, J.-H. Lee, Noble metal@ metal oxide semiconductor core@ shell nano-architectures as a new platform for gas sensor applications, RSC Adv. 5 (2015) 76229-76248, https://doi.org/10.1039/C5RA14322E.

[31] A. Mirzaei, K. Janghorban, B. Hashemi, G. Neri, Metal-core@ metal oxide-shell nanomaterials for gas-sensing applications: a review, J. Nanopart. Res. 17 (2015) 1-36, https://doi.org/10.1007/s11051-015-3164-5.

[32] K.Y. Shin, A. Mirzaei, H.Y. Lee, J.H. Bang, W. Oum, E.B. Kim, H.M. Kim, S.M. Majhi, S.S. Kim, H.W. Kim, Formation of nanograined Ag-Co_3O_4 core@ shell structure to achieve enhanced xylene sensing characteristics, Sens. Actuator B-Chem. (2023) 134049, https://doi.org/10.1016/j.snb.2023.134049.

[33] Z. Zhu, J.-L. Chang, R.-J. Wu, Fast ozone detection by using a core–shell Au@ TiO_2 sensor at room temperature, Sens. Actuator B-Chem. 214 (2015) 56-62, https://doi.org/10.1016/j.snb.2015.03.017.

[34] Y.-S. Kim, P. Rai, Y.-T. Yu, Microwave assisted hydrothermal synthesis of Au@ TiO_2 core–shell nanoparticles for high temperature CO sensing applications, Sens. Actuator B-Chem. 186 (2013) 633-639, https://doi.org/10.1016/j.snb.2013.06.038.

[35] J.-S. Park, Y.-S. Kim, P. Rai, Y.-T. Yu, Effect of Crystallinity of TiO_2 in Au@ TiO_2 Core–Shell Nanoparticles on CO Sensing Properties, Sens. Lett. 12 (2014) 1213-1217, https://doi.org/10.1166/sl.2014.3293.

[36] X. Yang, H. Fu, L. Zhang, X. An, S. Xiong, X. Jiang, A. Yu, Enhanced gas sensing performance based on the fabrication of polycrystalline Ag@ TiO_2 core-shell nanowires, Sens. Actuator B-Chem. 286 (2019) 483-492, https://doi.org/10.1016/j.snb.2019.01.096.

[37] Z. Zhu, C.-T. Kao, R.-J. Wu, A highly sensitive ethanol sensor based on Ag@TiO_2 nanoparticles at room temperature, Appl. Surf. Sci. 320 (2014) 348-355, https://doi.org/10.1016/j.apsusc.2014.09.108.

[38] H. Liu, W. Yang, M. Wang, L. Xiao, S. Liu, Fabrication of lotus-like Au@TiO_2 nanocomposites with enhanced gas-sensing properties, Sens. Actuator B-Chem. 236 (2016) 490-498, https://doi.org/10.1016/j.snb.2016.06.039.

[39] L.-Y. Zhu, L.-X. Ou, L.-W. Mao, X.-Y. Wu, Y.-P. Liu, H.-L. Lu, Advances in noble metal-decorated metal oxide nanomaterials for chemiresistive gas sensors: overview, Nano-Micro Lett. 15 (2023) 89, https://doi.org/10.1007/s40820-023-01047-z.

[40] H. Wu, L. Wang, J. Zhang, Z. Shen, J. Zhao, Catalytic oxidation of benzene, toluene and p-xylene over colloidal gold supported on zinc oxide catalyst, Catal. Commun. 12 (2011) 859-865, https://doi.org/10.1016/j.catcom.2011.02.012.

[41] H. Wu, L. Wang, Z. Shen, J. Zhao, Catalytic oxidation of toluene and p-xylene using gold supported on Co_3O_4 catalyst prepared by colloidal precipitation method, J. Mol. Catal. A-Chem. 351 (2011) 188-195, https://doi.org/10.1016/j.molcata.2011.10.005.

[42] S. Xie, Y. Liu, J. Deng, X. Zhao, J. Yang, K. Zhang, Z. Han, H. Arandiyan, H. Dai, Effect of transition metal doping on the catalytic performance of Au–Pd/3DOM Mn_2O_3 for the oxidation of methane and o-xylene, Appl. Catal. B-Environ. 206 (2017) 221-232, https://doi.org/10.1016/j.apcatb.2017.01.030.

[43] L.H.T. Nguyen, S.T. Navale, D.H. Yang, H.T.T. Nguyen, T.B. Phan, J.-Y. Kim, A. Mirzaei, T.L.H. Doan, S.S. Kim, H.W. Kim, Fe-based metal-organic framework as a chemiresistive sensor for low-temperature monitoring of acetone gas, Sens. Actuator B-Chem. 388 (2023) 133799, https://doi.org/10.1016/j.snb.2023.133799.

[44] S.K. Das, A.R. Das, A.K. Guha, Microbial synthesis of multishaped gold nanostructures, Small 6 (2010) 1012-1021, https://doi.org/10.1002/smll.200902011.

[45] K. Usha, P. Kumbhakar, B. Mondal, Effect of Ag-doped TiO_2 thin film passive layers on the performance of photo-anodes for dye-sensitized solar cells, Mater. Sci. Semicond. Process 43 (2016) 17-24, https://doi.org/10.1016/j.mssp.2015.11.015.

[46] E.M. El Mouchtari, L. El Mersly, O. Jhabli, H. Anane, A. Piram, S. Briche, P. Wong-Wah-Chung, S. Rafqah, Hydrothermal synthesis of 3D cauliflower anatase TiO_2 and bio sourced activated carbon: Adsorption and photocatalytic activity in real water matrices, Int. J. Environ. Anal. Chem. (2022) 1-16, https://doi.org/10.1080/03067319.2022.2118586.

[47] S. Li, A. Liu, Z. Yang, J. He, J. Wang, F. Liu, H. Lu, X. Yan, P. Sun, X. Liang, Room temperature gas sensor based on tin dioxide@ polyaniline nanocomposite assembled on

flexible substrate: ppb-level detection of NH_3, Sens. Actuator B-Chem. 299 (2019) 126970, https://doi.org/10.1016/j.snb.2019.126970.

[48] S. Yang, J. Sun, L. Xu, Q. Zhou, X. Chen, S. Zhu, B. Dong, G. Lu, H. Song, Au@ZnO functionalized three–dimensional macroporous WO_3: A application of selective H_2S gas sensor for exhaled breath biomarker detection, Sens. Actuator B-Chem. 324 (2020) 128725, https://doi.org/10.1016/j.snb.2020.128725.

[49] Z. Yang, L. Jiang, J. Wang, F. Liu, J. He, A. Liu, S. Lv, R. You, X. Yan, P. Sun, Flexible resistive NO_2 gas sensor of three-dimensional crumpled MXene $Ti_3C_2T_x$/ZnO spheres for room temperature application, Sens. Actuator B-Chem. 326 (2021) 128828, https://doi.org/10.1016/j.snb.2020.128828.

[50] L. Liu, Y. Wang, K. Guan, Y. Liu, Y. Li, F. Sun, X. Wang, C. Zhang, S. Feng, T. Zhang, Influence of oxygen vacancies on the performance of SnO_2 gas sensing by near-ambient pressure XPS studies, Sens. Actuator B-Chem. 393 (2023) 134252, https://doi.org/10.1016/j.snb.2023.13425.

[51] M. Al-Hashem, S. Akbar, P. Morris, Role of oxygen vacancies in nanostructured metal-oxide gas sensors: a review, Sens. Actuator B-Chem. 301 (2019) 126845, https://doi.org/10.1016/j.snb.2019.126845.

[52] X. Kou, F. Meng, K. Chen, T. Wang, P. Sun, F. Liu, X. Yan, Y. Sun, F. Liu, K. Shimanoe, High-performance acetone gas sensor based on Ru-doped SnO_2 nanofibers, Sens. Actuator B-Chem. 320 (2020) 128292, https://doi.org/10.1016/j.snb.2020.128292.

[53] H.W. Kim, Y.J. Kwon, A. Mirzaei, S.Y. Kang, M.S. Choi, J.H. Bang, S.S. Kim, Synthesis of zinc oxide semiconductors-graphene nanocomposites by microwave irradiation for application to gas sensors, Sens. Actuator B-Chem. 249 (2017) 590-601, https://doi.org/10.1016/j.snb.2017.03.149.

[54] S. Guo, S.D. Wolf, M. Sitti, C. Serre, S.C. Tan, Hygroscopic Materials. Adv. Mater. 36 (2024) 2311445, https://doi.org/10.1002/adma.202311445.

[55] K.Y. Shin, L.H.T. Nguyen, H.L. Nguyen, A. Mirzaei, V.N.H. Tran, N.X.D. Mai, N.Q. Tran, W. Oum, E.B. Kim, H.M. Kim, Titanium-based metal-organic-framework-coated SnO_2 nanowires with enhanced NO_2 gas sensing capability in humid environment, Sens. Actuator B-Chem. 394 (2023) 134425, https://doi.org/10.1016/j.snb.2023.134425.

[56] G. Niu, F. Wang, A review of MEMS-based metal oxide semiconductors gas sensor in Mainland China, J. Micromech. Microeng. 32 (2022) 054003, https://doi.org/10.1088/1361-6439/ac5b98.

[57] J. Wang, H. Shen, Y. Xia, S. Komarneni, Light-activated room-temperature gas sensors based on metal oxide nanostructures: A review on recent advances, Ceram. Int. 47 (2021) 7353-7368, https://doi.org/10.1016/j.ceramint.2020.11.187.

[58] P. Bharathi, S. Harish, M. Shimomura, M.K. Mohan, J. Archana, M. Navaneethan, Ultrasensitive and reversible NO_2 gas sensor based on SnS_2/TiO_2 heterostructures for room temperature applications, Chemosphere 346 (2024) 140486, https://doi.org/10.1016/j.chemosphere.2023.140486.

[59] A. Mirzaei, J.-H. Kim, H.W. Kim, S.S. Kim, How shell thickness can affect the gas sensing properties of nanostructured materials: Survey of literature, Sens. Actuator B-Chem. 258 (2018) 270-294, https://doi.org/10.1016/j.snb.2017.11.066.

[60] V. Amiri, H. Roshan, A. Mirzaei, G. Neri, A.I. Ayesh, Nanostructured metal oxide-based acetone gas sensors: A review, Sensors 20 (2020) 3096, https://doi.org/10.3390/s20113096.

[61] K. Xu, Y. Yang, T. Yu, C. Yuan, WO_3 nanofibers anchored by porous $NiCo_2O_4$ nanosheets for xylene detection, Ceram. Int. 44 (2018) 21717-21724, https://doi.org/10.1016/j.ceramint.2018.08.261.

[62] S. Navale, A. Mirzaei, S.M. Majhi, H.W. Kim, S.S. Kim, State-of-the-art research on chemiresistive gas sensors in korea: Emphasis on the achievements of the research labs of professors Hyoun Woo Kim and Sang Sub Kim, Sensors 22 (2021) 61, https://doi.org/10.3390/s22010061.

[63] R. Ranjithkumar, P. Lakshmanan, N. Palanisami, P. Devendran, N. Nallamuthu, S. Sudhahar, M.K. Kumar, Facile, Morphology-Controlled and Mass Production of 0D-Ag/2D-g-C_3N_4/3D-TiO_2 Nano-composite Materials: Effect of Silver Morphology and Loading on the Electrochemical Performance, Electron. Mater. Lett. 19 (2023) 172-183, https://doi.org/10.1007/s13391-022-00385-1.

[64] S. Lee, E.-J. Yun, Effects of Bismuth Doping on the Properties of CuO_x Thin Films, Electron. Mater. Lett. 19 (2023) 1-7, https://doi.org/10.1007/s13391-023-00408-5.

[65] O. Lupan, V. Postica, N. Ababii, T. Reimer, S. Shree, M. Hoppe, O. Polonskyi, V. Sontea, S. Chemnitz, F. Faupel, Ultra-thin TiO_2 films by atomic layer deposition and surface functionalization with Au nanodots for sensing applications, Mater. Sci. Semicond. Process 87 (2018) 44-53, https://doi.org/10.1016/j.mssp.2018.06.031.

[66] J.-H. Kim, I. Sakaguchi, S. Hishita, T. Ohsawa, T.T. Suzuki, N. Saito, Self-heated CO gas sensor based on Au-decorated Sb-implanted WS_2 nanosheets, Sens. Actuator B-Chem. 382 (2023) 133501, https://doi.org/10.1016/j.snb.2023.133501.

[67] D.J. Yu, W. Oum, A. Mirzaei, K.Y. Shin, E.B. Kim, H.M. Kim, S.S. Kim, H.W. Kim, Enhancement of xylene gas sensing by using Au core structures in regard to Au@ SnO_2 core-shell nanocomposites, Sens. Actuator B-Chem. 392 (2023) 134018, https://doi.org/10.1016/j.snb.2023.134018.

[68] J. Huang, H. Liang, J. Ye, D. Jiang, Y. Sun, X. Li, Y. Geng, J. Wang, Z. Qian, Y. Du, Ultrasensitive formaldehyde gas sensor based on Au-loaded ZnO nanorod arrays at low temperature, Sens. Actuator B-Chem. 346 (2021) 130568, https://doi.org/10.1016/j.snb.2021.130568.

[69] F. Li, S. Ruan, N. Zhang, Y. Yin, S. Guo, Y. Chen, H. Zhang, C. Li, Synthesis and characterization of Cr-doped WO_3 nanofibers for conductometric sensors with high xylene sensitivity, Sens. Actuator B-Chem. 265 (2018) 355-364, https://doi.org/10.1016/j.snb.2018.03.054.

[70] L. Liu, Z. Zhong, Z. Wang, L. Wang, S. Li, Z. Liu, Y. Han, Y. Tian, P. Wu, X. Meng, Synthesis, Characterization, and m- Xylene Sensing Properties of Co–ZnO Composite Nanofibers, J. Am. Ceram. Soc. 94 (2011) 3437-3441, https://doi.org/10.1111/j.1551-2916.2011.04528.x.

[71] Z. Lin, J. Gong, P. Fu, Hierarchical Fe_2O_3/Bi_2WO_6 nanoplates with enhanced xylene sensing performance, J. Mater. Sci.-Mater. Electron. 28 (2017) 4424-4430, https://doi.org/10.1007/s10854-016-6071-3.

[72] C. Feng, C. Wang, H. Zhang, X. Li, C. Wang, P. Cheng, J. Ma, P. Sun, Y. Gao, H. Zhang, Enhanced sensitive and selective xylene sensors using W-doped NiO nanotubes, Sens. Actuator B-Chem. 221 (2015) 1475-1482, https://doi.org/10.1016/j.snb.2015.07.114.

[73] H. Qin, Y. Cao, J. Xie, H. Xu, D. Jia, Solid-state chemical synthesis and xylene-sensing properties of α-MoO_3 arrays assembled by nanoplates, Sens. Actuator B-Chem. 242 (2017) 769-776, https://doi.org/10.1016/j.snb.2016.11.081.

[74] F. Qu, H. Jiang, M. Yang, Designed formation through a metal organic framework route of $ZnO/ZnCo_2O_4$ hollow core–shell nanocages with enhanced gas sensing properties, Nanoscale 8 (2016) 16349-16356, https://doi.org/10.1039/C6NR05187A.

[75] L. Sui, X. Zhang, X. Cheng, P. Wang, Y. Xu, S. Gao, H. Zhao, L. Huo, Au-loaded hierarchical MoO_3 hollow spheres with enhanced gas-sensing performance for the detection of BTX (benzene, toluene, and xylene) and the sensing mechanism, ACS Appl. Mater. Interfaces 9 (2017) 1661-1670, https://doi.org/10.1021/acsami.6b11754.

[76] H. Gao, Q. Yu, S. Zhang, T. Wang, P. Sun, H. Lu, F. Liu, X. Yan, F. Liu, X. Liang, Nanosheet-assembled NiO microspheres modified by Sn^{2+} ions isovalent interstitial doping for xylene gas sensors, Sens. Actuator B-Chem. 269 (2018) 210-222, https://doi.org/10.1016/j.snb.2018.04.161.

[77] D. Jiang, W. Wei, F. Li, Y. Li, C. Liu, D. Sun, C. Feng, S. Ruan, Xylene gas sensor based on α-MoO_3/α-Fe_2O_3 heterostructure with high response and low operating temperature, RSC Adv. 5 (2015) 39442-39448, https://doi.org/10.1039/C5RA05661F.

[78] C. Fàbrega, O. Casals, F. Hernández-Ramírez, J. Prades, A review on efficient self-heating in nanowire sensors: Prospects for very-low power devices, Sens. Actuator B-Chem. 256 (2018) 797-811, https://doi.org/10.1016/j.snb.2017.10.003.

[79] E. Espid, F. Taghipour, UV-LED photo-activated chemical gas sensors: A review, Crit. Rev. Solid State Mat. Sci. 42 (2017) 416-432, https://doi.org/10.1080/10408436.2016.122616.

[80] S. Zhang, Y. Deng, A. Libanori, Y. Zhou, J. Yang, T. Tat, L. Yang, W. Sun, P. Zheng, Y.L. Zhu, In situ grown silver–polymer framework with coordination complexes for functional artificial tissues, Adv. Mater. 35 (2023) 2207916, https://doi.org/10.1002/adma.202207916.

[81] S. Zhang, Y. Zhou, A. Libanori, Y. Deng, M. Liu, M. Zhou, H. Qu, X. Zhao, P. Zheng, Y.-L. Zhu, Biomimetic spinning of soft functional fibres via spontaneous phase separation, Nat. Electron. 6 (2023) 338-348, https://doi.org/10.1038/s41928-023-00960-w.

Figure Captions

Fig. 1. Schematics of the synthesis of Au-TiO_2 C-S NPs and the fabrication of the sensing device.

Fig. 2. (a)-(c) TEM images of Au-TiO_2 C-S NPs at different magnifications, (d) SAED pattern, (e-(h) TEM-EDS color mapping analysis, and (i) EDS spectrum of Au-TiO_2 C-S NPs.

Fig. 3. XRD patterns of the (a) Au-TiO_2 C-S NPs and (b) TiO_2 NPs. The standard JCPDS patterns of (c) TiO_2 and (d) Au. SEM images of (e,f) TiO_2 NPs and (g,h) Au-TiO_2 C-S NPs at different magnifications.

Fig. 4. N_2 adsorption-desorption curves of (a) TiO_2 NPs and (b) Au-TiO_2 C-S NPs and BJH plot of (c) TiO_2 NPs and (d) Au-TiO_2 C-S NPs.

Fig. 5. XPS survey of Au-TiO_2 C-S NPs. XPS core levels of (b) Au 4f, (c) Ti 2p, and (d) O1s.

Fig. 6. (a) Normalized UPS spectra of Au and TiO_2 NPs. Energy cut-off values of (b) Au and (c) TiO_2 NPs.

Fig. 7. (a) Responses of TiO_2 and Au-TiO_2 C-S NPs gas sensors to 50 ppm xylene gas versus temperature. Variations of the resistance of (b) pristine TiO_2 and (c) Au-TiO_2 C-S nanocomposite gas sensors with varying the temperature.

Fig. 8. Dynamic resistance curves of (a) TiO_2 and (b) Au-TiO_2 C-S NP gas sensors to 10, 30, and 50 ppm xylene gas at 450°C. Comparison of gas performance of TiO_2 and Au-TiO_2 C-S NP gas sensors to 10, 30, and 50 ppm xylene gas at 450°C. (c) Dynamic response curves and (d) sensor response.

Fig. 9. Dynamic resistance curves of Au-TiO_2 C-S NPs to 1, 3, 5, 7, and 9 ppm xylene gas at 450°C. (b) Corresponding calibration curve, (c) selectivity histogram of TiO_2 and Au-TiO_2 C-S

NP gas sensors to 50 ppm gases at 450°C, and (d) dynamic relative responses of Au-TiO_2 C-S NP gas sensors to 50 ppm gases at 450°C in the presence of 0, 40, and 80% RH. RH was set and measured at 25°C. (e) Repeatability test showing five sequential cycles of Au-TiO_2 C-S NPs gas sensor exposed to 50 ppm xylene gas at 450°C, and (f) corresponding response values plotted against the sensing cycles. (g) Reproducibility test for three similarly prepared Au-TiO_2 C-S NPs gas sensors exposed to 50 ppm xylene gas at 450°C, (h) dynamic response curves comparing fresh and six-month-preserved Au-TiO_2 C-S NPs gas sensors exposed to 50 ppm xylene gas at 450°C.

Fig. 10. Schematic of the xylene sensing mechanism of the Au-TiO_2 C-S NP gas sensor.

Fig. 11. Energy bands of TiO_2 and Au (a) before contact and after contact in (b) air and (c) xylene gas.

Table 1. The xylene sensing properties of Au-TiO_2 C-S NPs and those reported in the literature.

Sensing material	**Conc. (ppm)**	**T(°C)**	**Response (R_a/ R_g) or (R_g/R_a)**	**Ref.**
Au-SnO_2 nanocomposite	100	350	27.9	[67]
$NiCo_2O_4$/WO_3 nanocomposite	100	300	15.7	[61]
Cr-doped WO_3 nanofiber	100	225	35	[69]
0.4 wt% Co-doped ZnO nanofiber	100	320	14.8	[70]
10 wt% α-Fe_2O_3/Bi_2WO_6 nanoplate	100	260	13.5	[71]
W-doped NiO nanotube	200	375	8.74	[72]
α-MoO_3 nanoplates	100	370	19.2	[73]
ZnO/$ZnCo_2O_4$ hollow C-S nanocage	100	320	34.26	[74]
Au-loaded MoO_3 hollow sphere	100	250	22.1	[75]
Sn-doped NiO microsphere	10	250	3	[76]
α-MoO_3/α-Fe_2O_3 heterojunction	100	206	6.8	[77]
Au-TiO_2 C-S NPs	**50**	**450**	**165.77**	**Present work**

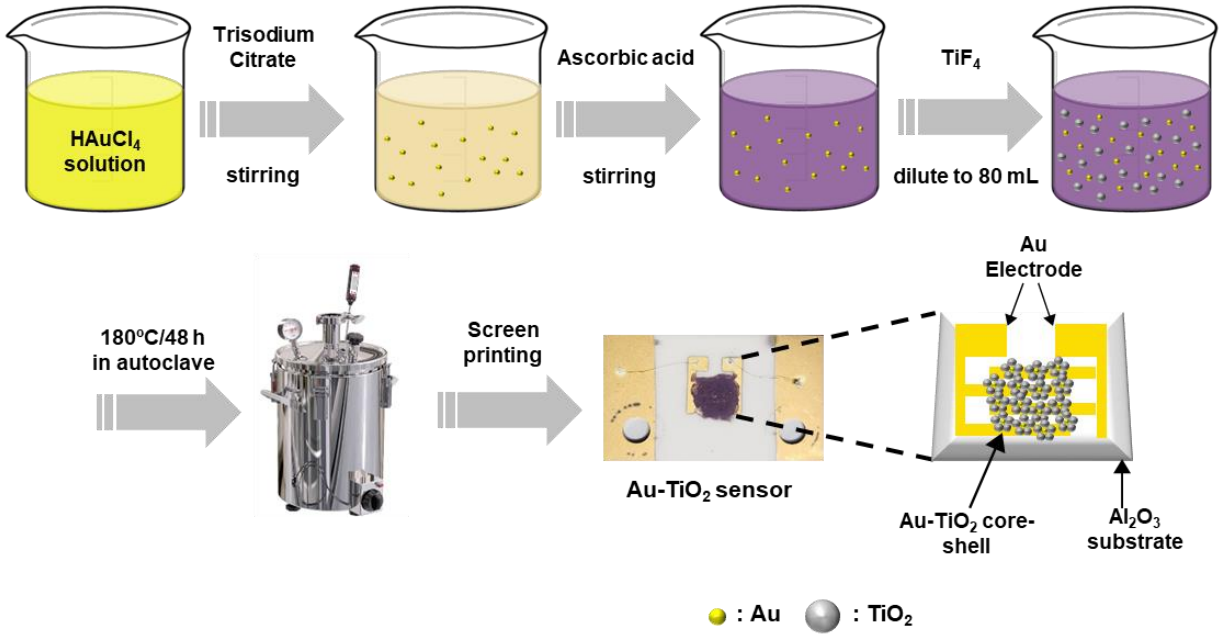
HAuCl4 solution
Trisodium Citrate
stirring
Ascorbic acid
stirring
TiF4
dilute to 80 mL
180°C/48 h in autoclave
Screen printing
Au Electrode
Au-TiO2 sensor
Au-TiO2 core-shell
Al2O3 substrate
: Au
: TiO2

Fig. 1

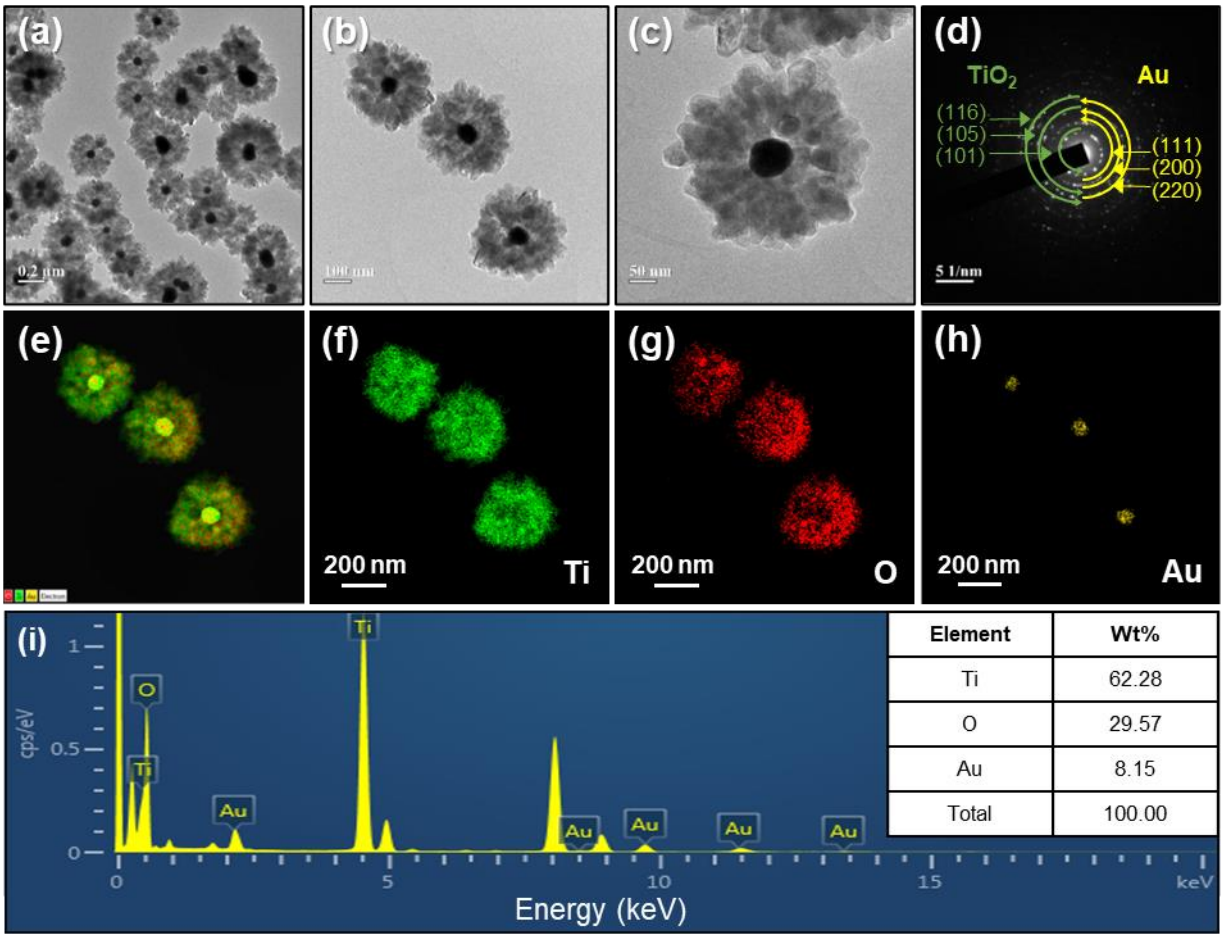
(a)
0.2 μm
(b)
100 nm
(c)
50 nm
(d)
TiO2
Au
(116)
(105)
(101)
(111)
(200)
(220)
5 1/nm
(e)
(f)
200 nm
Ti
(g)
200 nm
O
(h)
200 nm
Au
(i)
cps/eV
Energy (keV)
keV
Element
Wt%
Ti
62.28
O
29.57
Au
8.15
Total
100.00

Fig. 2

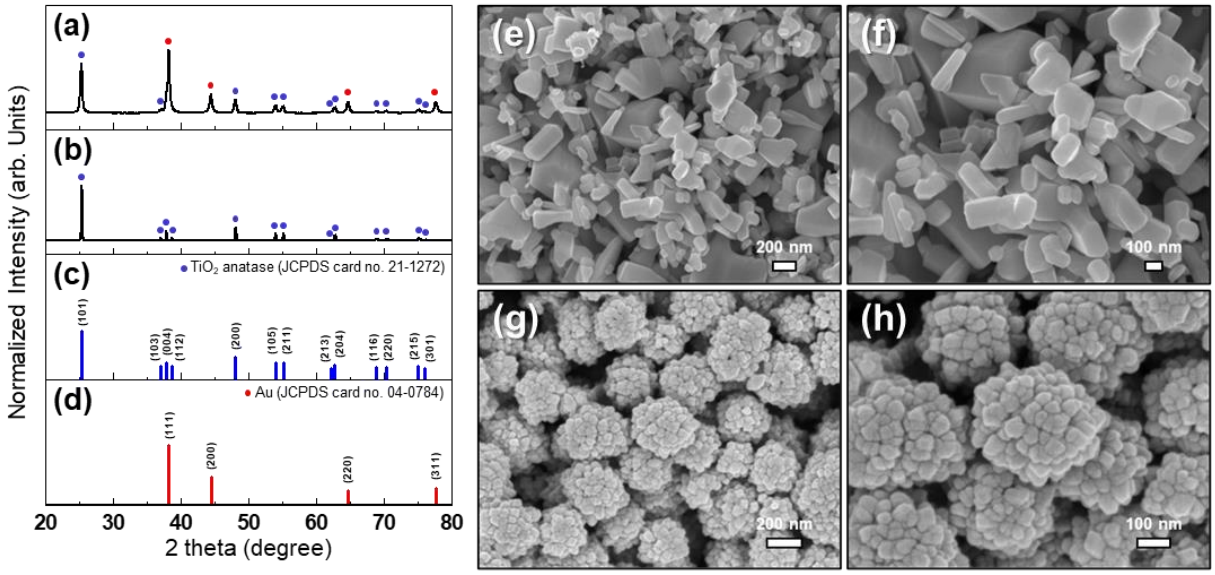
(a)
(b)
(c)
(d)
Normalized Intensity (arb. Units)
TiO2 anatase (JCPDS card no. 21-1272)
(101)
(103)
(004)
(112)
(200)
(105)
(211)
(213)
(204)
(116)
(220)
(215)
(301)
Au (JCPDS card no. 04-0784)
(111)
(200)
(220)
(311)
20
30
40
50
60
70
80
2 theta (degree)
(e)
200 nm
(f)
100 nm
(g)
200 nm
(h)
100 nm

Fig. 3

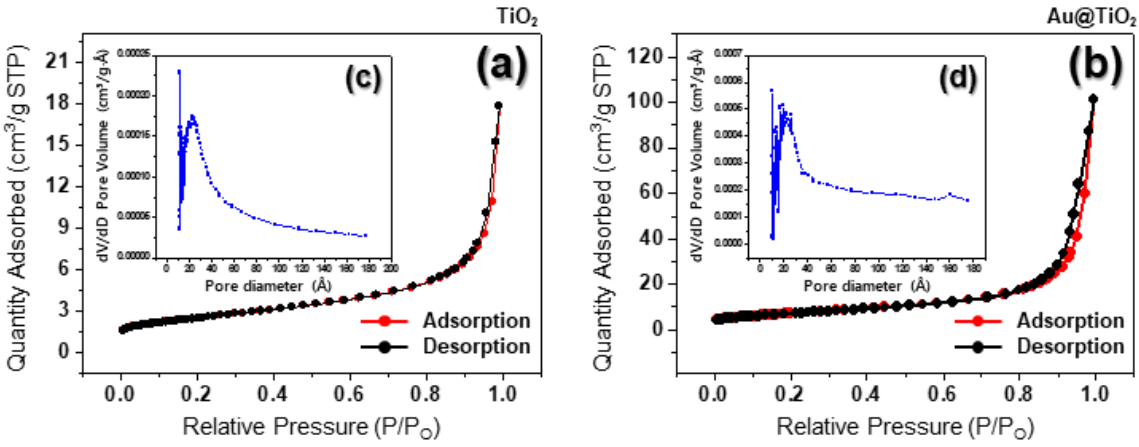
TiO2
(a)
(c)
Quantity Adsorbed (cm3/g STP)
Relative Pressure (P/Po)
dV/dD Pore Volume (cm3/g·Å)
Pore diameter (Å)
Adsorption
Desorption
Au@TiO2
(b)
(d)

Fig. 4

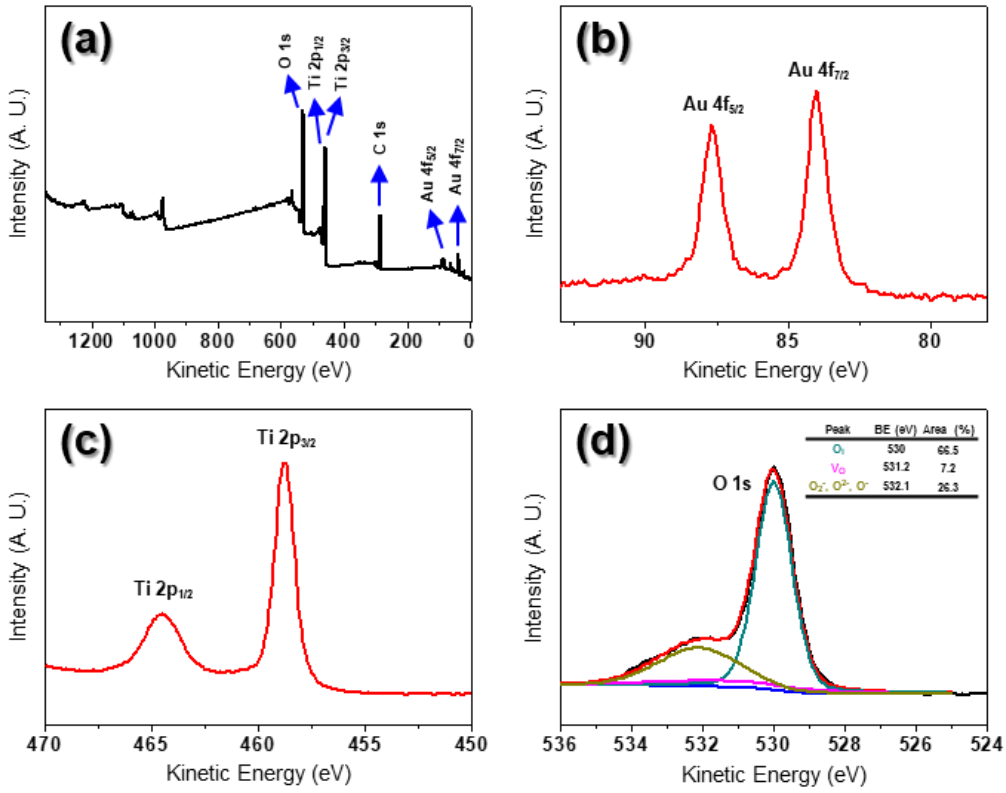
(a)
O 1s
Ti 2p1/2
Ti 2p3/2
C 1s
Au 4f5/2
Au 4f7/2
Intensity (A. U.)
1200 1000 800 600 400 200 0
Kinetic Energy (eV)
(b)
Au 4f5/2
Au 4f7/2
Intensity (A. U.)
90 85 80
Kinetic Energy (eV)
(c)
Ti 2p3/2
Ti 2p1/2
Intensity (A. U.)
470 465 460 455 450
Kinetic Energy (eV)
(d)
O 1s
Peak BE (eV) Area (%)
OI 530 66.5
VO 531.2 7.2
O2-, O2-, O- 532.1 26.3
Intensity (A. U.)
536 534 532 530 528 526 524
Kinetic Energy (eV)

Fig. 5

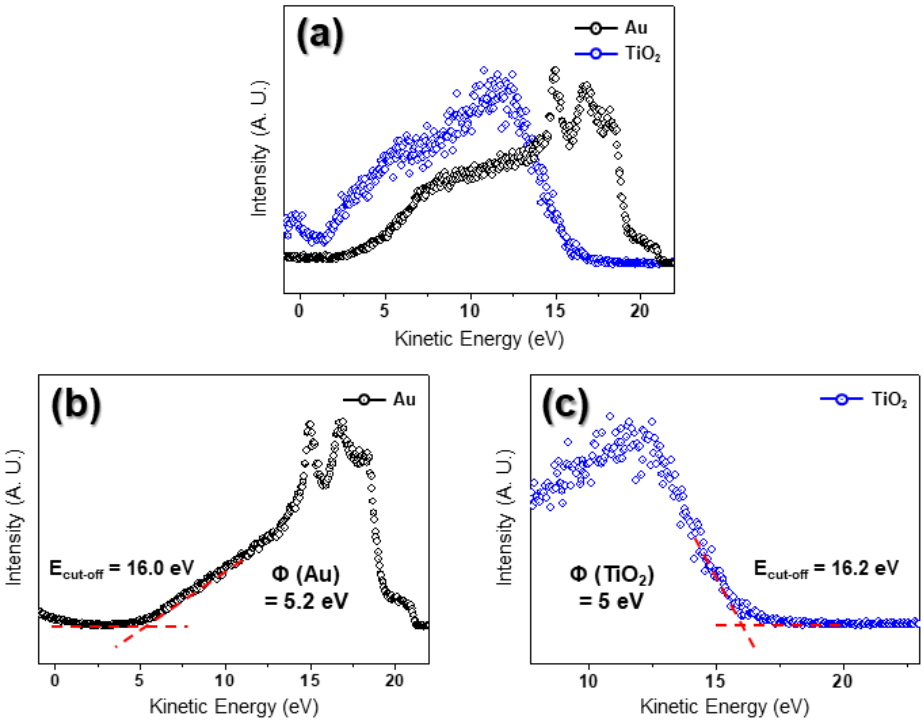
(a)
Au
TiO2
Intensity (A. U.)
0
5
10
15
20
Kinetic Energy (eV)
(b)
Au
Intensity (A. U.)
Ecut-off = 16.0 eV
Φ (Au)
= 5.2 eV
0
5
10
15
20
Kinetic Energy (eV)
(c)
TiO2
Intensity (A. U.)
Φ (TiO2)
= 5 eV
Ecut-off = 16.2 eV
10
15
20
Kinetic Energy (eV)

Fig. 6

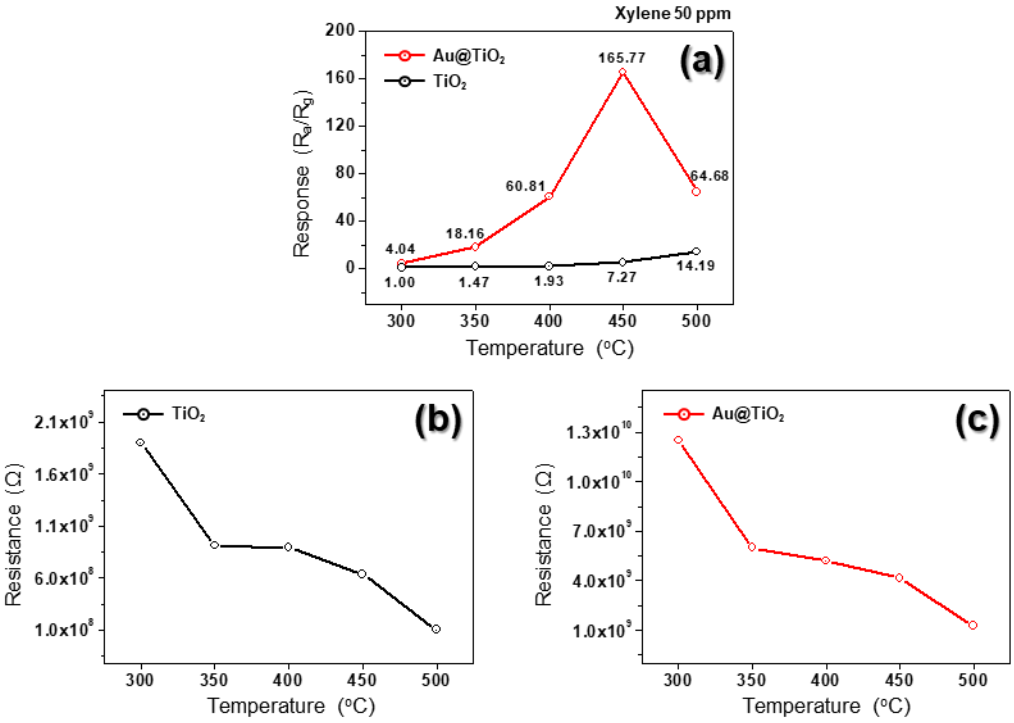
Xylene 50 ppm
(a)
Au@TiO2
TiO2
Response (Ra/Rg)
165.77
64.68
60.81
18.16
4.04
1.00
1.47
1.93
7.27
14.19
Temperature (°C)
(b)
TiO2
Resistance (Ω)
Temperature (°C)
(c)
Au@TiO2
Resistance (Ω)
Temperature (°C)

Fig. 7

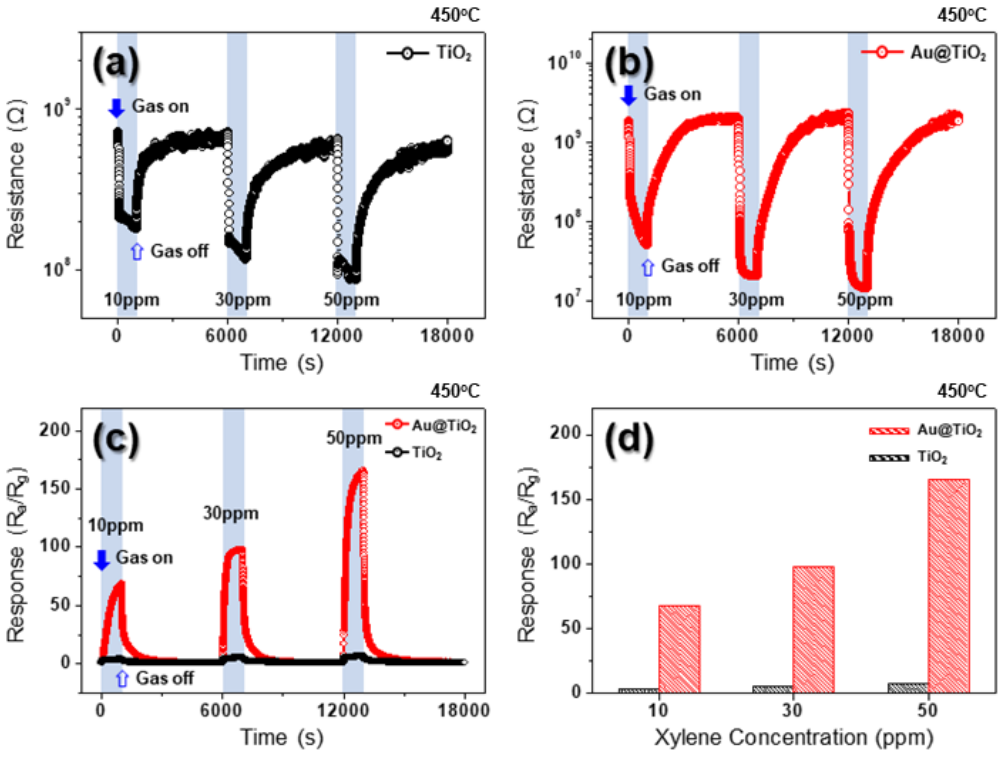
450°C
(a)
TiO2
Gas on
Gas off
10ppm
30ppm
50ppm
Resistance (Ω)
Time (s)
450°C
(b)
Au@TiO2
Gas on
Gas off
10ppm
30ppm
50ppm
Resistance (Ω)
Time (s)
450°C
(c)
Au@TiO2
TiO2
10ppm
30ppm
50ppm
Gas on
Gas off
Response (Rg/Rg)
Time (s)
450°C
(d)
Au@TiO2
TiO2
Response (Rg/Rg)
Xylene Concentration (ppm)

Fig. 8

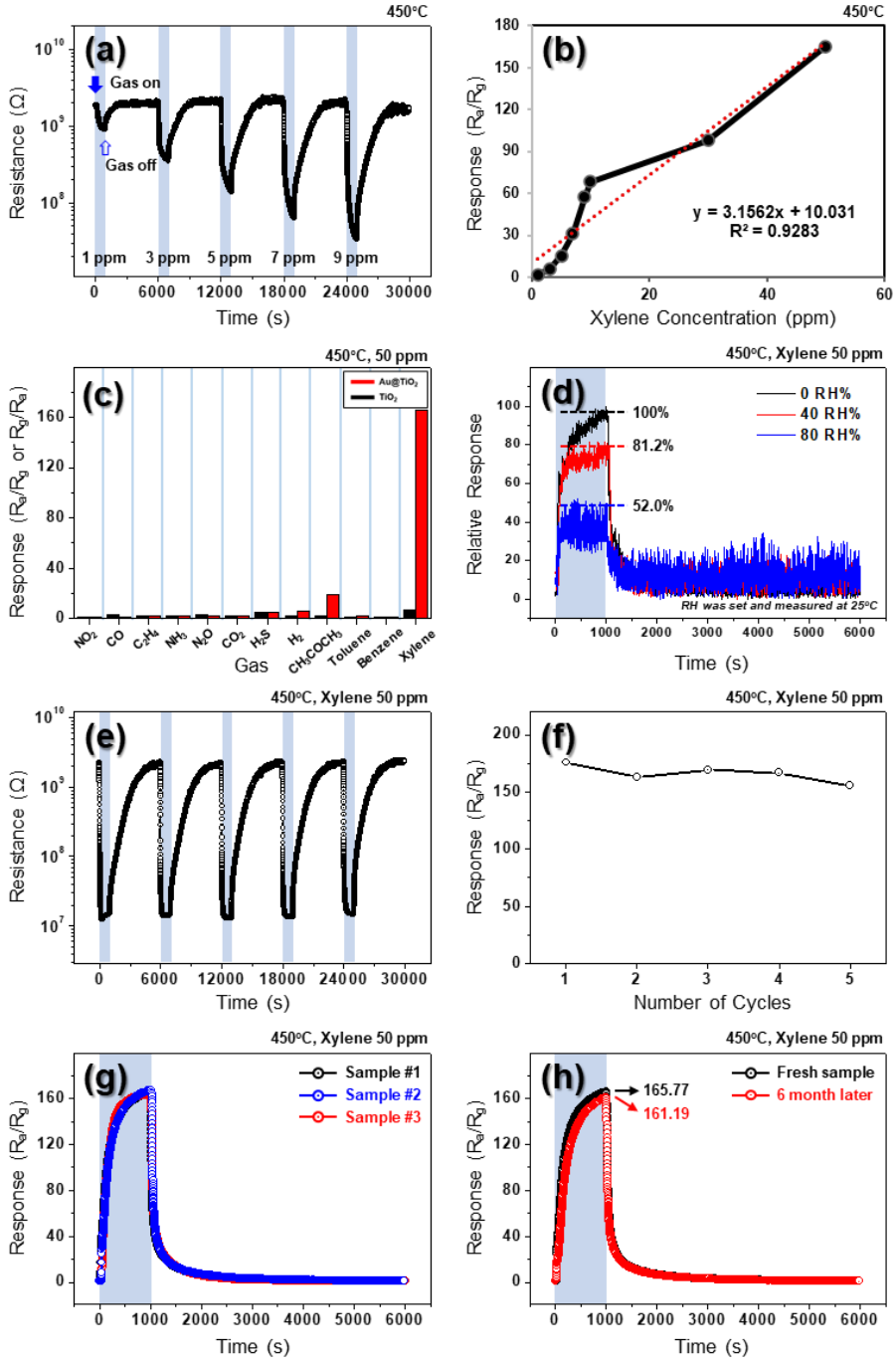
450°C
(a)
Gas on
Gas off
1 ppm
3 ppm
5 ppm
7 ppm
9 ppm
Resistance (Ω)
Time (s)
(b)
y = 3.1562x + 10.031
R² = 0.9283
Response (Ra/Rg)
Xylene Concentration (ppm)
450°C, 50 ppm
(c)
Au@TiO2
TiO2
Response (Ra/Rg or Rg/Ra)
NO2
CO
C2H4
NH3
N2O
CO2
H2S
H2
CH3COCH3
Toluene
Benzene
Xylene
Gas
450°C, Xylene 50 ppm
(d)
0 RH%
40 RH%
80 RH%
100%
81.2%
52.0%
RH was set and measured at 25°C
Relative Response
Time (s)
450°C, Xylene 50 ppm
(e)
Resistance (Ω)
Time (s)
450°C, Xylene 50 ppm
(f)
Response (Ra/Rg)
Number of Cycles
450°C, Xylene 50 ppm
(g)
Sample #1
Sample #2
Sample #3
Response (Ra/Rg)
Time (s)
450°C, Xylene 50 ppm
(h)
Fresh sample
6 month later
165.77
161.19
Response (Ra/Rg)
Time (s)

Fig. 9

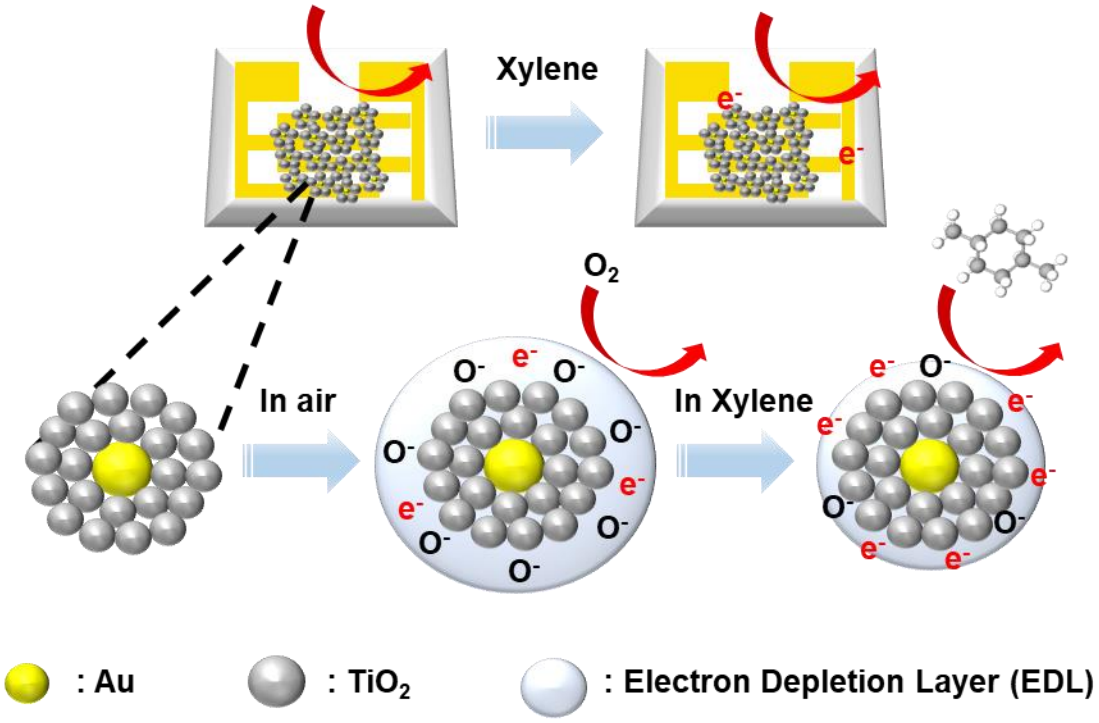
Xylene
e-
e-
O2
In air
In Xylene
O-
e-
: Au
: TiO2
: Electron Depletion Layer (EDL)

Fig. 10

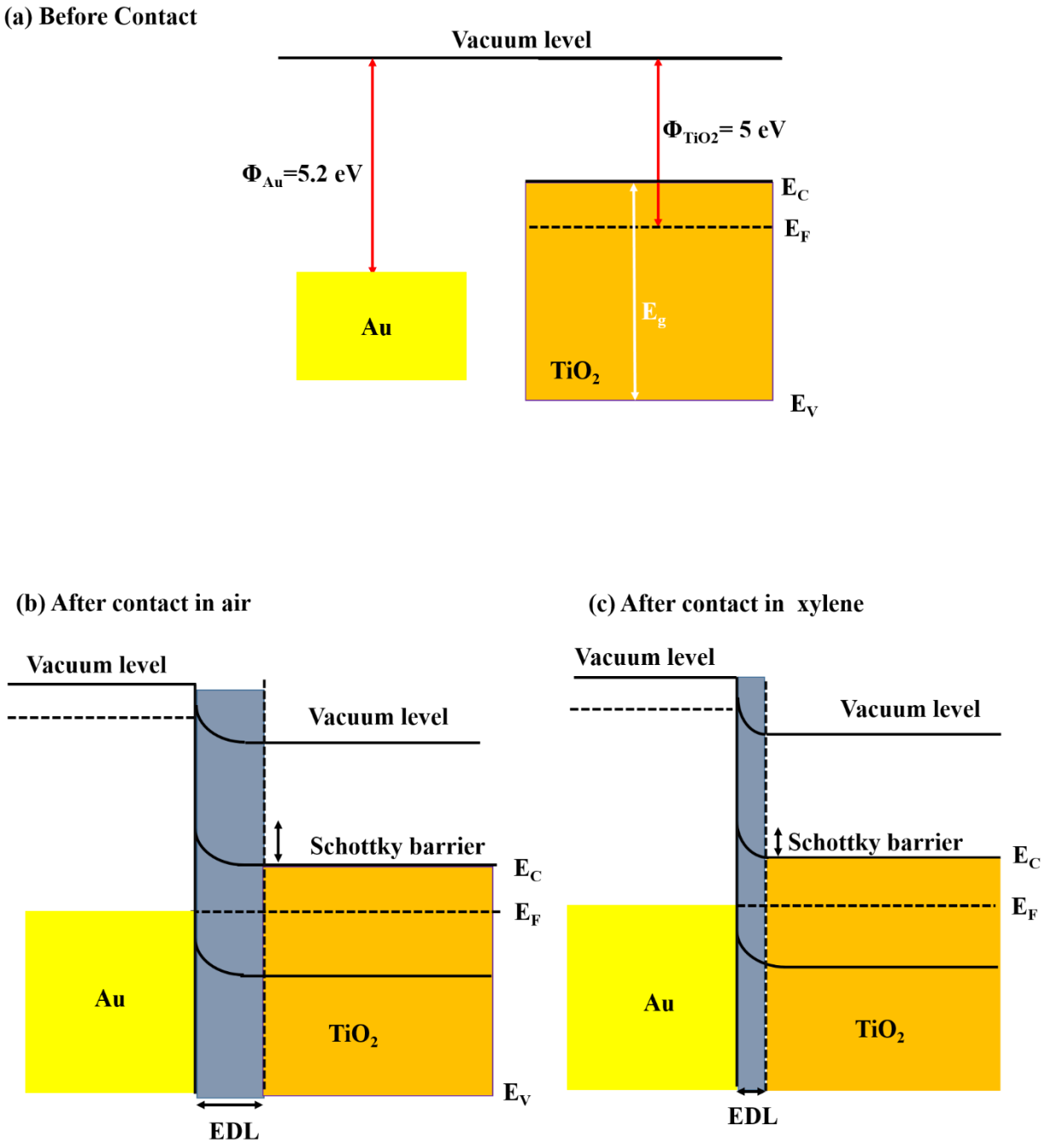
(a) Before Contact
Vacuum level
Φ_{Au}=5.2 eV
Φ_{TiO2}= 5 eV
Au
E_C
E_F
E_g
TiO_2
E_V
(b) After contact in air
Vacuum level
Vacuum level
Schottky barrier
E_C
E_F
Au
TiO_2
E_V
EDL
(c) After contact in xylene
Vacuum level
Vacuum level
Schottky barrier
E_C
E_F
Au
TiO_2
EDL

Fig. 11

Figure 1

Click here to access/download;Figure(s);Figure 1.tif

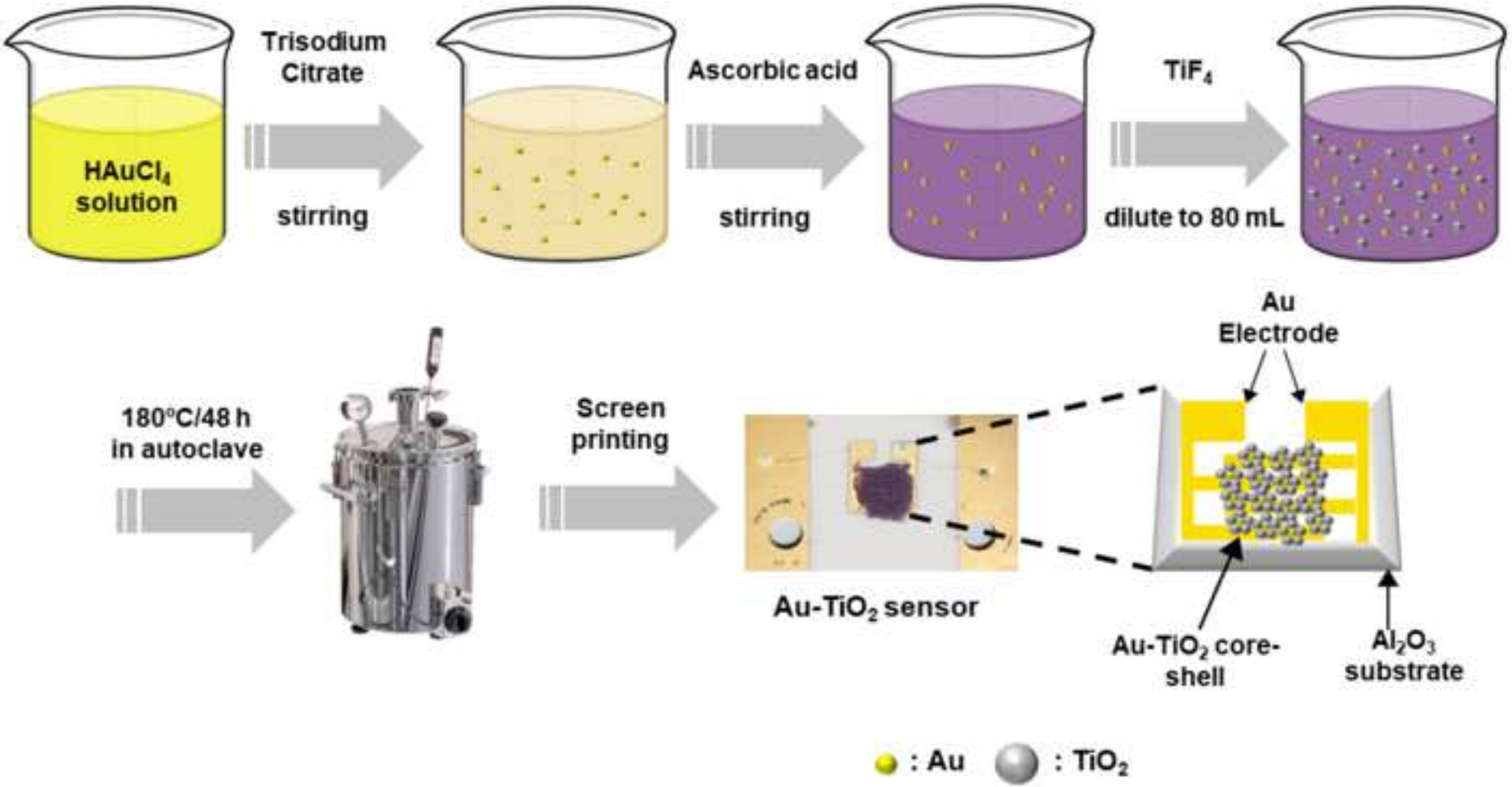

Figure 2

Click here to access/download;Figure(s);Figure 2.tif

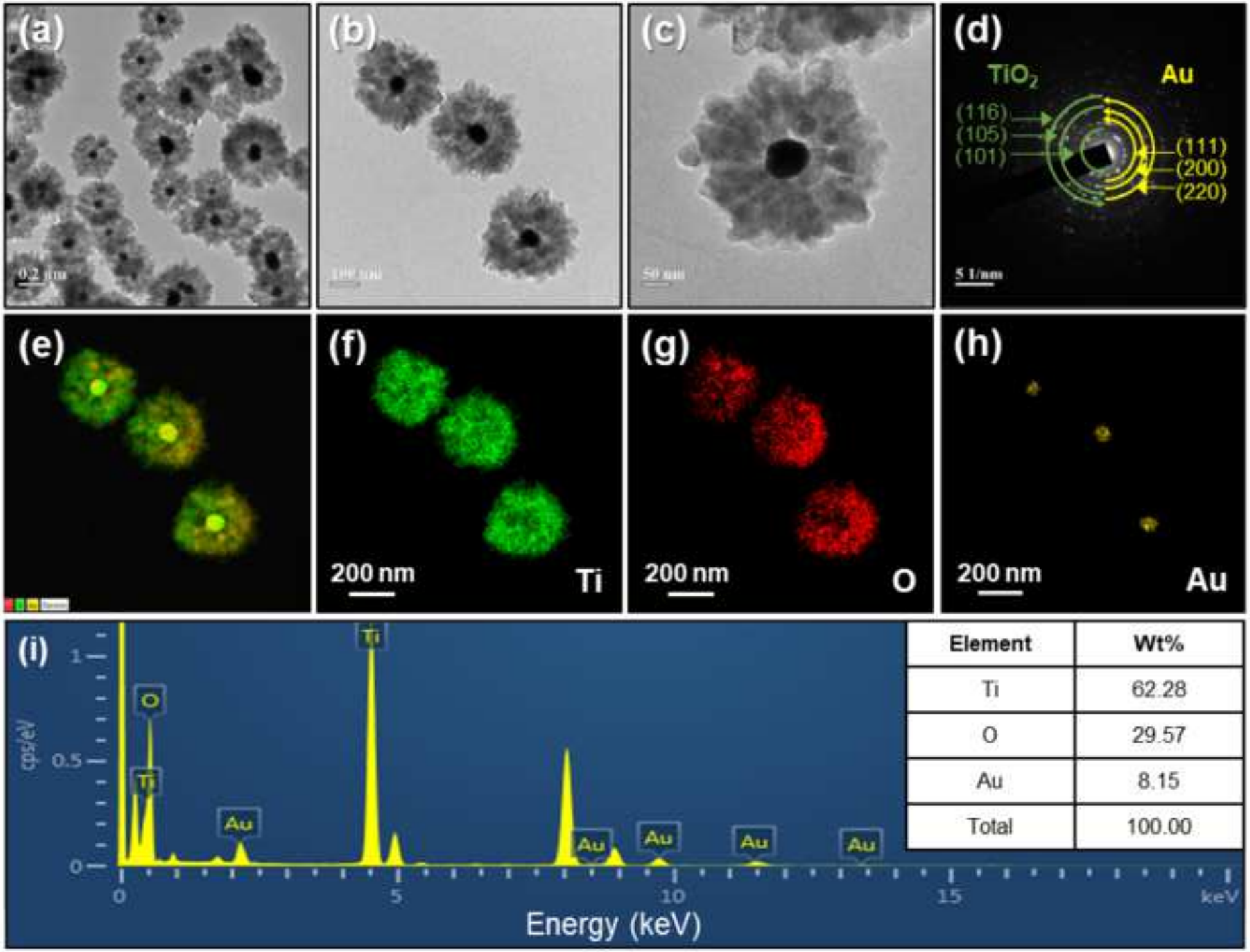

Element	Wt%
Ti	62.28
O	29.57
Au	8.15
Total	100.00

Figure 3

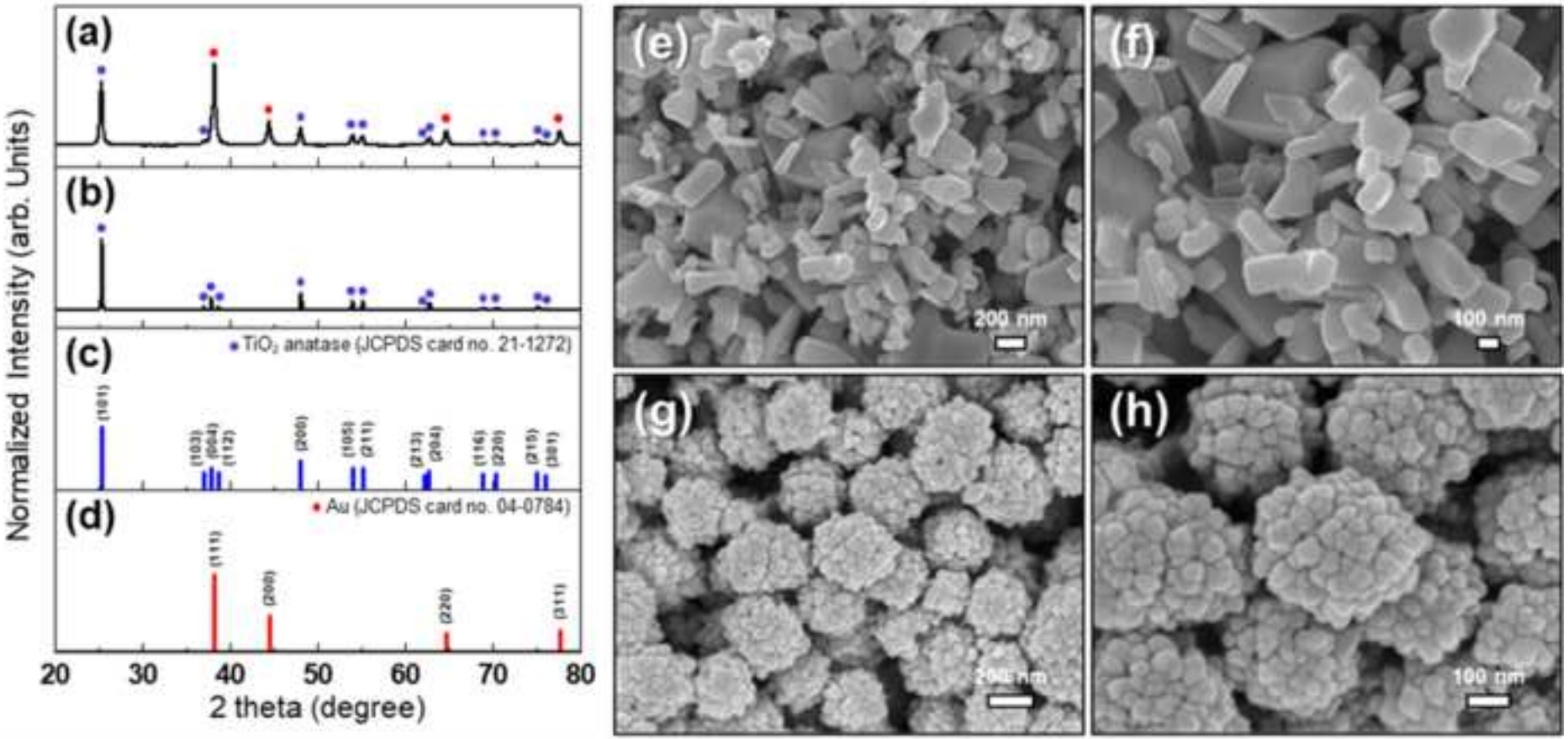

Figure 4

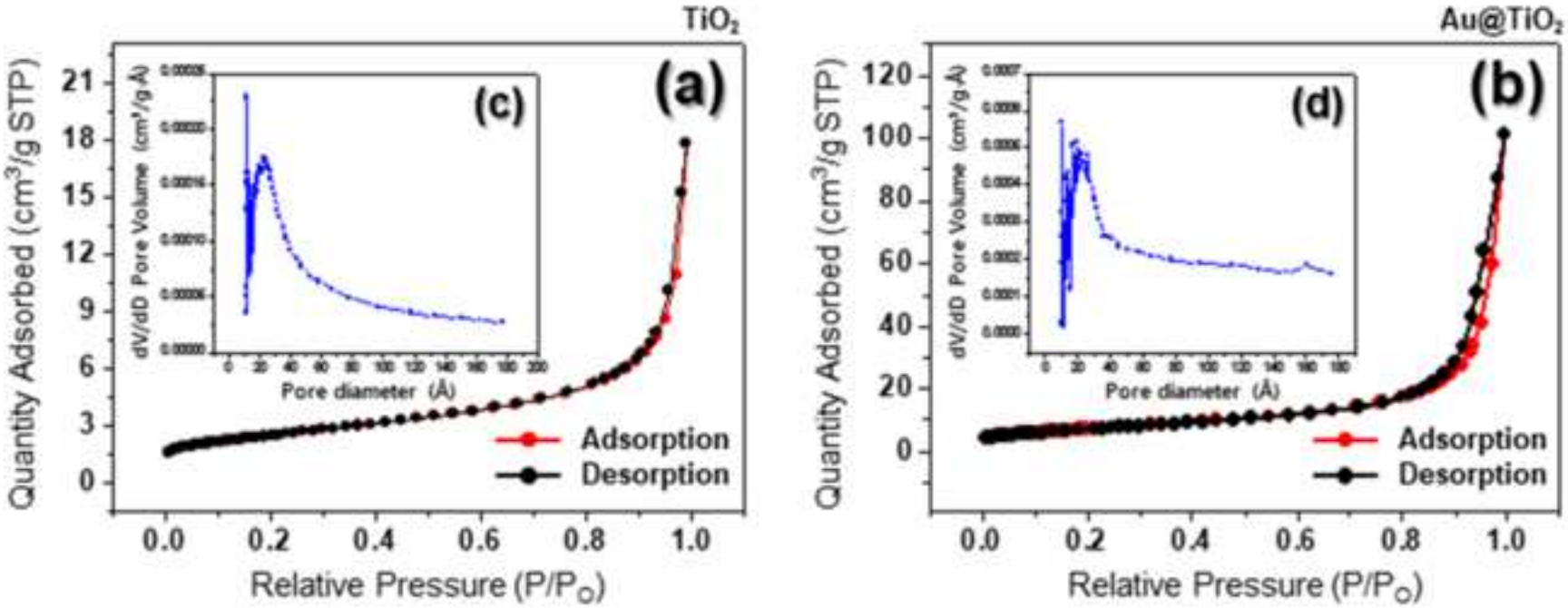

Figure 5

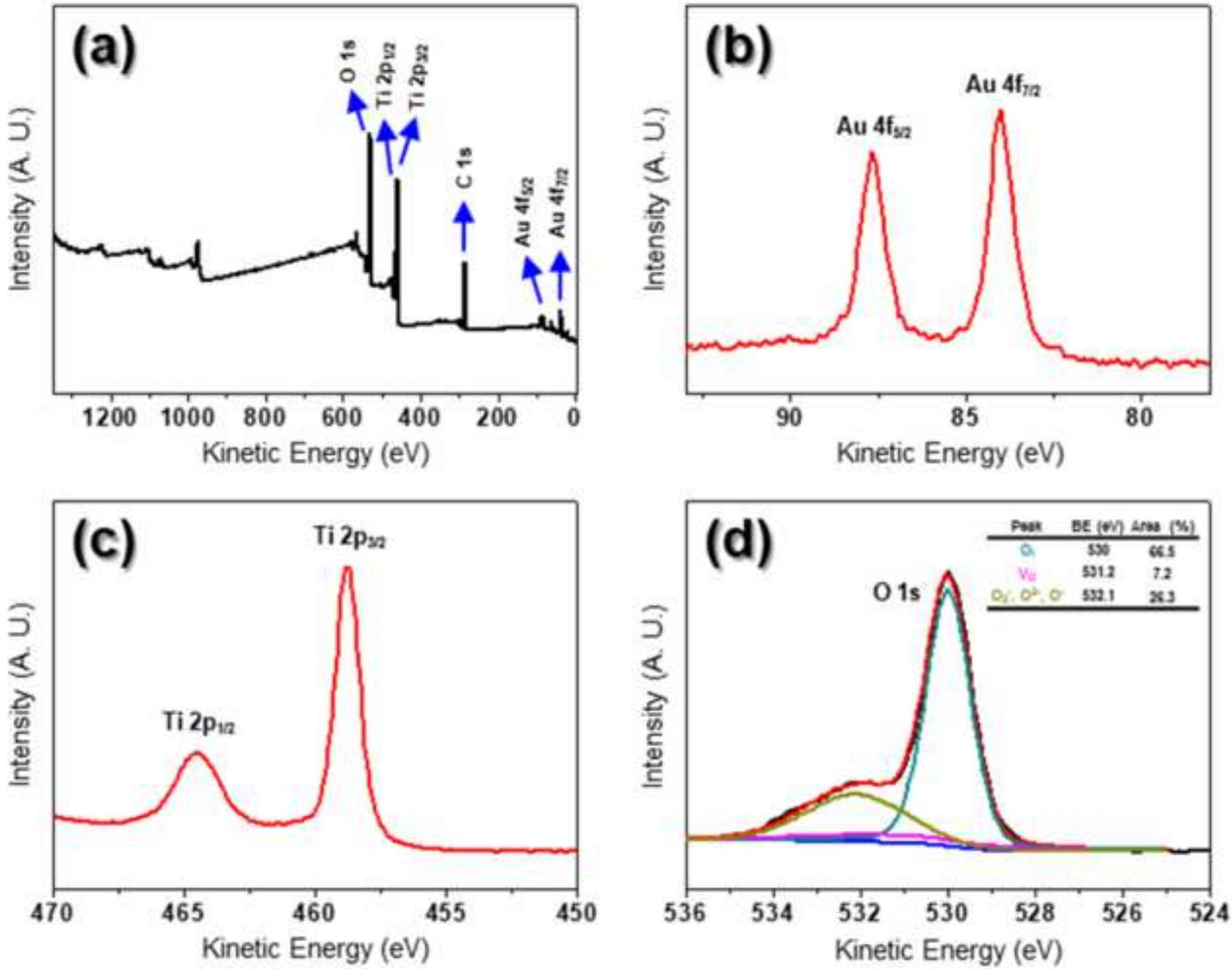

Figure 6

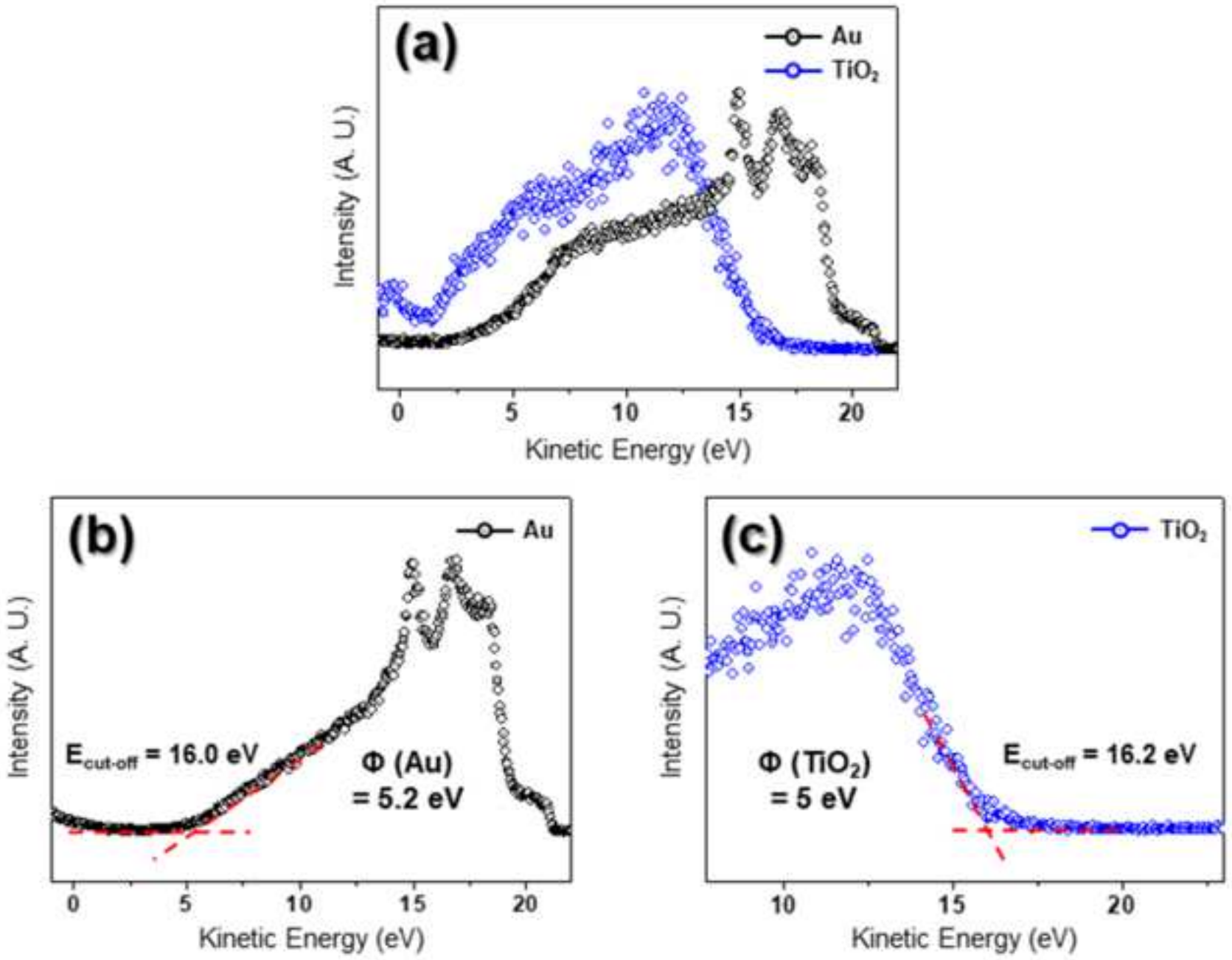

Figure 7

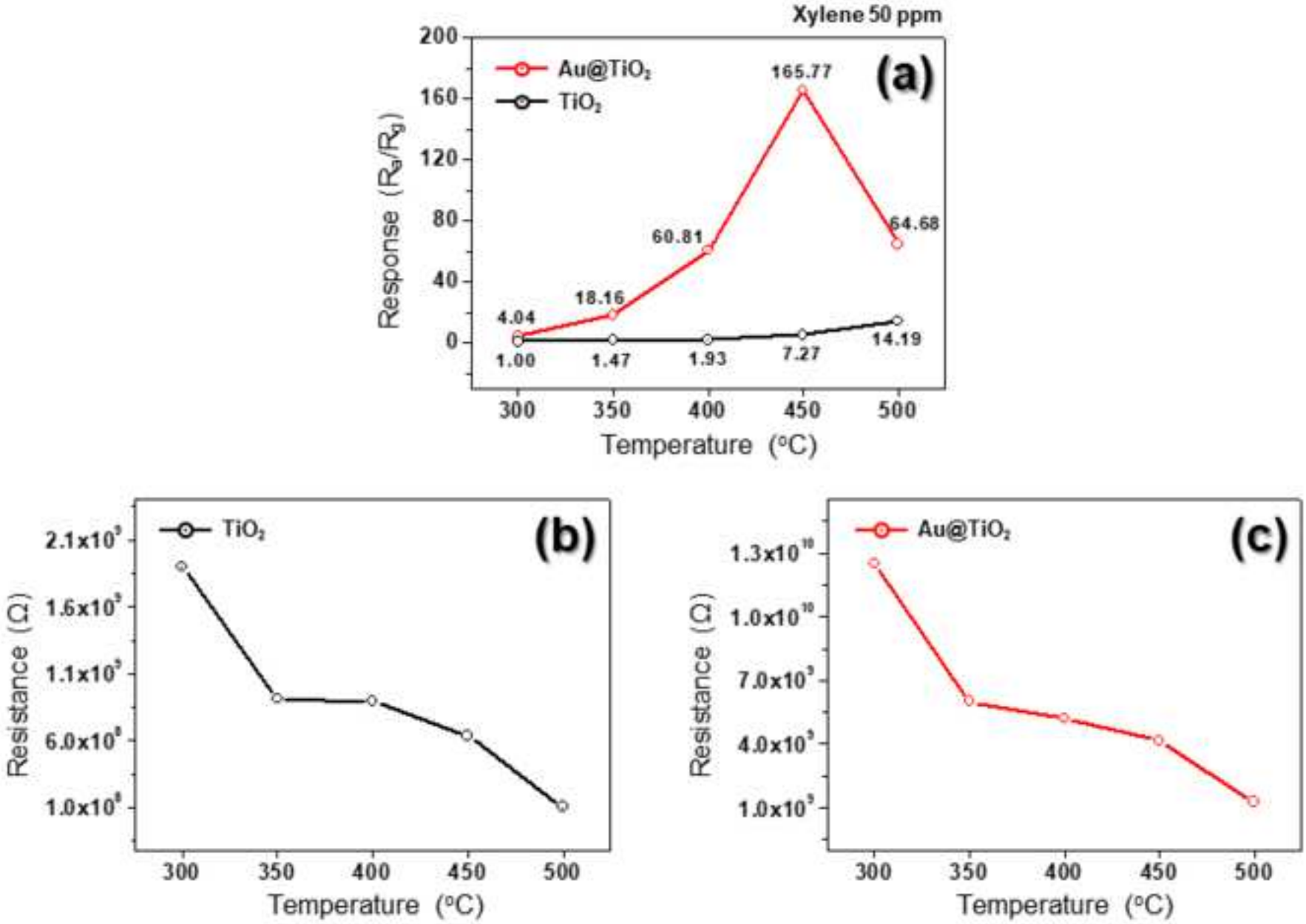

Figure 8

Click here to access/download;Figure(s);Figure 8.tif

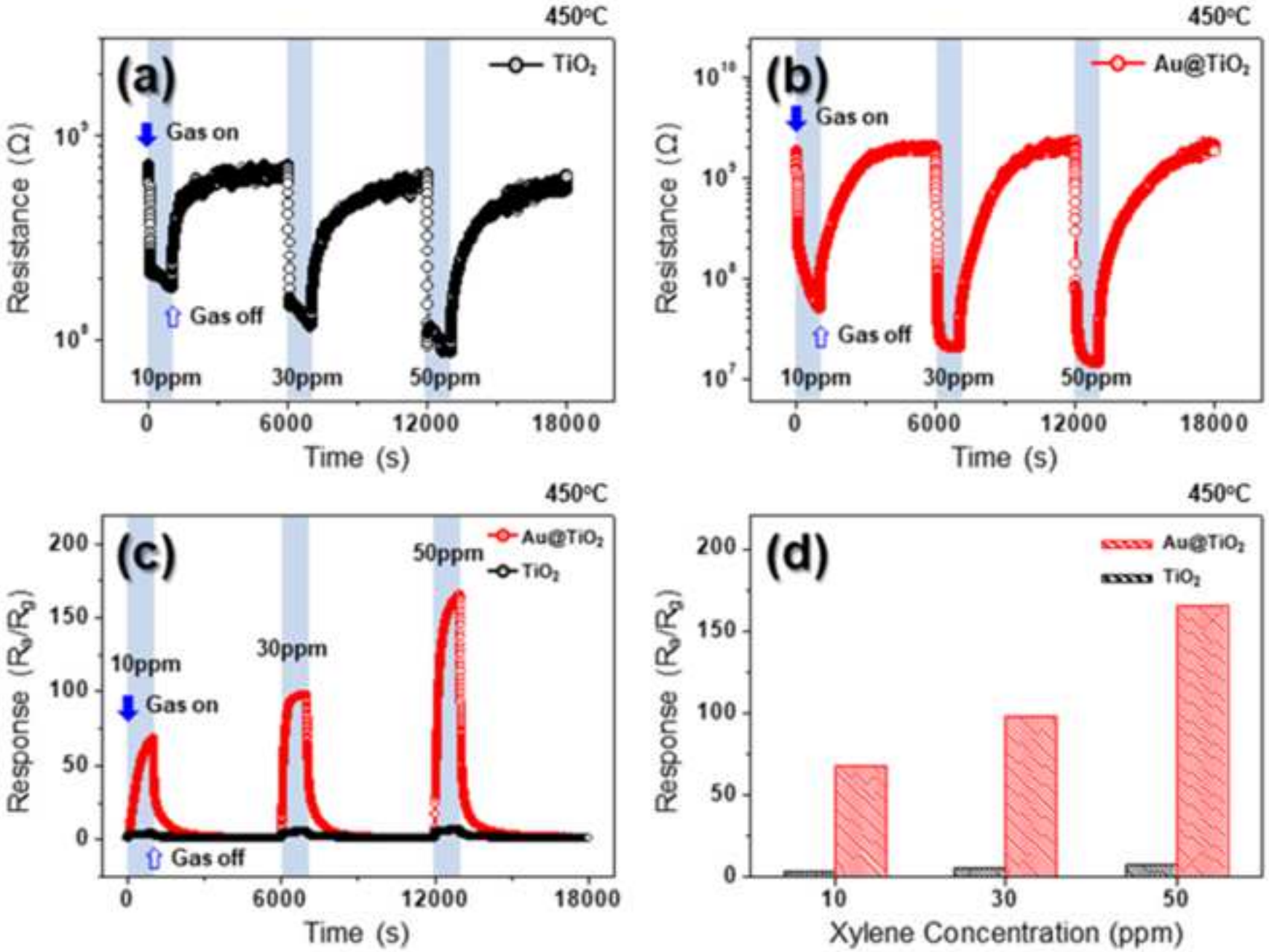

Figure 9

Click here to access/download;Figure(s);Figure 9.tif

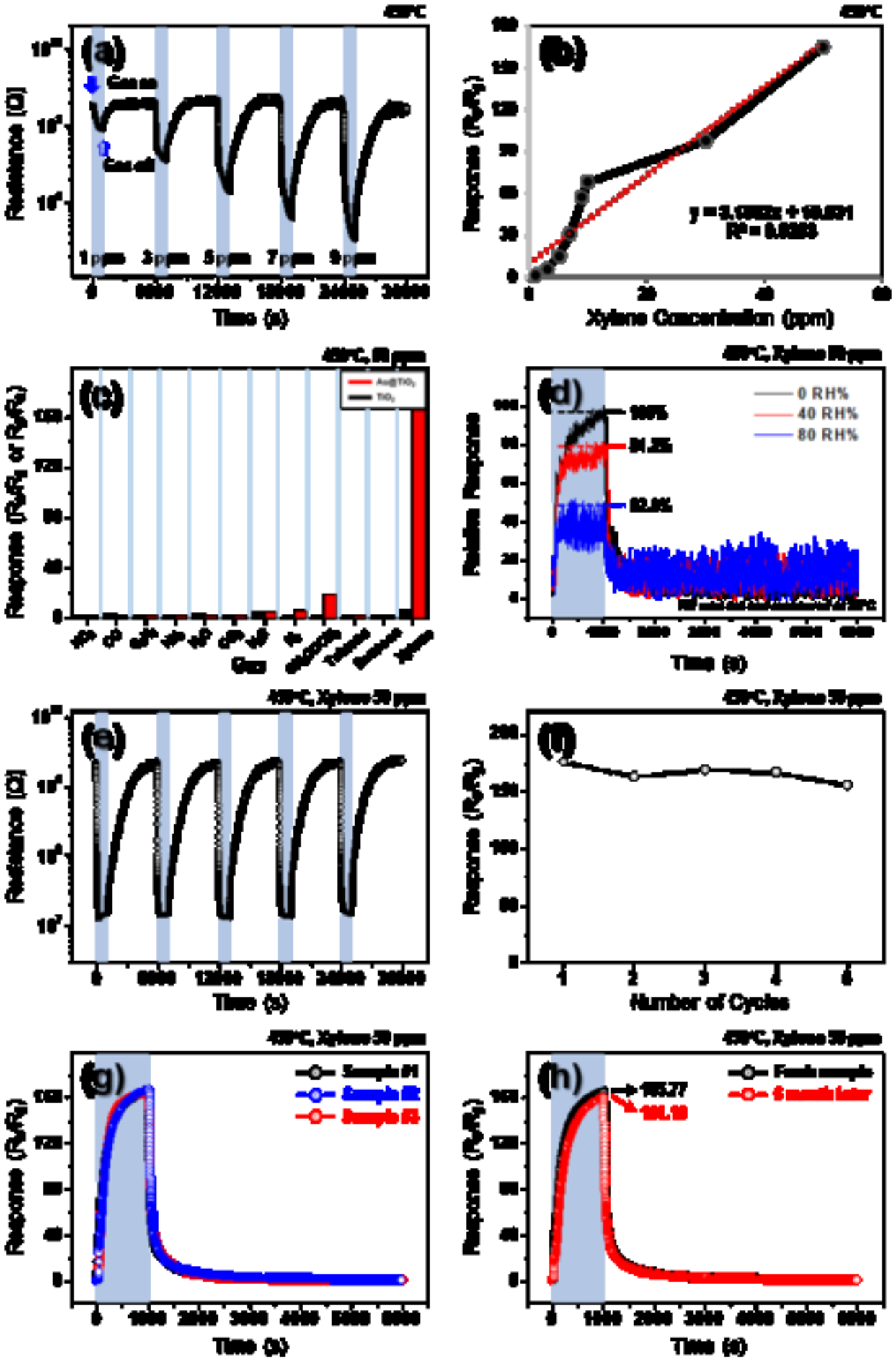

Figure 10